



Title	Impacts of Salinity Variation on the Mixed-Layer Processes and Sea Surface Temperature in the Kuroshio-Oyashio Confluence Region
Author(s)	Kido, Shoichiro; Nonaka, Masami; Tanimoto, Youichi
Citation	Journal of Geophysical Research Oceans, 126(8), e2020JC016914 https://doi.org/10.1029/2020JC016914
Issue Date	2021-08
Doc URL	http://hdl.handle.net/2115/83993
Rights	Copyright 2021 American Geophysical Union.
Type	article (author version)
File Information	Kido_et_al(2021)_KOCR_ori.pdf



[Instructions for use](#)

1 **Impacts of salinity variation on the mixed-layer processes**
2 **and sea surface temperature in the Kuroshio-Oyashio**
3 **confluence region**

4 **Shoichiro Kido¹**
5 **Masami Nonaka¹**
6 **Youichi Tanimoto^{1,2}**
7
8

9
10 **(4th revision)**
11

12 1: Application Laboratory (APL), Research Institute for Value-Added-Information Generation
13 (VAiG), Japan Agency for Marine-Earth Science and Technology (JAMSTEC), Yokohama, Japan
14

15 2: Faculty of Environmental Earth Science, Hokkaido University, Sapporo, Japan
16

17 Key points:

18 1. Coherent temperature and salinity variations are identified in the Kuroshio-Oyashio
19 confluence region during boreal winter to spring

20 2. The dynamical stability of the Kuroshio Extension is the key factor responsible for these
21 temperature and salinity variations

22 3. Changes in density field associated with salinity anomalies significantly affect the strength of
23 vertical mixing and sea surface temperature

24 **Abstract:**

25 In this study, salinity variations in the Kuroshio–Oyashio confluence region (KOCR) are
26 examined through analyses of observational datasets and an ocean reanalysis product, and their
27 potential impacts on sea surface temperature are assessed by sensitivity experiments using a one-
28 dimensional mixed layer model (1-D ML model). We have detected prominent covariations in
29 near surface temperature and salinity in the KOCR during the boreal winter to spring. Further
30 investigation revealed that such covariations are closely related to the dynamical stability of the
31 Kuroshio Extension (KE), and anomalous warming and saltening (cooling and freshening) are
32 observed in the KOCR when the upstream of the KE is in an unstable (a stable) state. It is found
33 that modulation heat and freshwater transport by mesoscale eddies and large-scale current
34 anomalies are closely related to such observed variation. Then, we have quantitatively estimated
35 the impacts of these salinity variations on local density by a detailed decomposition of total
36 anomaly fields. Although the total density anomalies are dominated by contributions from
37 temperature, the salinity contribution has sizable magnitude especially in the northern part of the
38 KOCR, where the background temperature is low and the dependence of density on temperature
39 variations is weak. To further quantify the impact of salinity anomalies, we conducted a series of
40 sensitivity experiments utilizing the 1-D ML model. The results from these experiments revealed
41 that salinity anomalies significantly alter the strength of vertical mixing and eventually lead to
42 differences in sea surface temperature of approximately 1.0 °C.

43 (245 words < 250 words)

44

45 **Plain Language summary:**

46 The Kuroshio–Oyashio confluence region (KOCR) in the western North Pacific Ocean
47 undergoes well-defined low-frequency variation on interannual to decadal time scales, and play a
48 pivotal role in the climate variability of the North Pacific. Although significant progress has been
49 made in understanding the dynamical and thermodynamical characteristics of the KOCR
50 variations, less attention has been paid to salinity variability. With the variation in the density of
51 seawater, salinity can potentially exert significant effects on various physical processes in the
52 upper ocean. Therefore, it is important to properly describe its features and assess its possible
53 impacts. In pursuit of these objectives, herein we investigate salinity variations in the KOCR and
54 its possible impacts through analysis of observational datasets and sensitivity experiments using
55 a simplified model. We found that the upper ocean temperature and salinity in the KOCR exhibit
56 distinct covariation during boreal winter, and they are primarily caused by modulations of ocean
57 circulation in the same region. A detailed decomposition of density anomalies and numerical
58 experiments demonstrated that these salinity anomalies significantly affect the strength of
59 vertical mixing and sea surface temperature, suggesting that salinity has a potential to play an
60 active role in low-frequency variations of the KOCR.

61 **(199 words < 200 words)**

62

63 **1. Introduction**

64 The upper ocean circulation in the western North Pacific is characterized by two
65 remarkable western boundary currents, namely the Kuroshio and Oyashio, which constitute the
66 subtropical and subarctic gyres, respectively (Fig. 1a) (Qiu, 2002; Yasuda, 2003). Warm and
67 saline subtropical water is transported poleward by the Kuroshio, whereas cold and fresh water
68 from the subpolar region is advected equatorward by the Oyashio. After separating from the
69 coast of Japan, these western boundary currents and associated water masses meet together to
70 form the Kuroshio–Oyashio confluence region (KOCR). Due to the marked differences in the
71 physical properties of these water masses, the hydrographic structures of the KOCR are far from
72 uniform and many complicated but intriguing features, such as sharp sea surface temperature
73 (SST) and salinity (SSS) fronts (Figs. 1b, c), vigorous submesoscale/mesoscale eddies, as well as
74 abrupt changes in vertical stratification (Fig. 1d) are observed (Kida et al., 2015; Roden, 1972; I.
75 Yasuda, 2003; Yuan & Talley, 1996).

76 The oceanic variables (e.g. temperature, salinity, sea surface height (SSH), and current
77 fields) in the KOCR undergo significant variations on various time scales, and interannual to
78 decadal variability in surface and subsurface temperature is especially strong near the
79 climatological fronts (Figs. 1e, f) (Nakamura et al., 1997; Nakamura & Kazmin, 2003; Nonaka et
80 al., 2006). As SST fronts in the KOCR affect the baroclinicity of the lower troposphere and
81 anchor the latitude of the extratropical storm tracks (Nakamura et al., 2004), changes in the
82 KOCR SST not only significantly modulate the local atmospheric conditions but also exert
83 substantial effects on large-scale atmospheric circulation (Frankignoul et al., 2011; Kwon et al.,
84 2010; Ma et al., 2015; Smirnov et al., 2015; Taguchi et al., 2012). The KOCR is also known as a
85 key region for water mass formation. Reflecting the intricate hydrographic structures, strong
86 horizontal gradients of the mixed layer depth (MLD) can be seen in the KOCR (Fig. 1d), and

87 they also experience large low-frequency variations as well as other oceanic parameters (Fig. 1f)
88 (Oka et al., 2012; Suga et al., 2004). The inhomogeneous distribution of the MLD in the KOCR
89 is conducive to the formation of mode waters, which are characterized by vertically uniform
90 water properties and believed to play an important role in long-term climate variability and
91 biogeochemical processes. Indeed, various types of mode water are formed in the vicinity of the
92 KOCR, such as the subtropical mode water (Masuzawa, 1969), central mode water (Suga et al.,
93 1997), and transition region mode water (Saito et al., 2007), and their variations are closely
94 linked to the variability of the KOCR (see review by Oka & Qiu, 2012). For these reasons, a
95 comprehensive description and understanding of oceanic variations in the KOCR are of
96 particular interests from various perspectives.

97 Thanks to the progress of observational platforms and numerical ocean models in recent
98 decades, significant advances have been made in understanding the driving mechanisms of
99 oceanic variations in the KOCR and other western boundary current regions (Kelly et al., 2010;
100 Kwon et al., 2010). In particular, many studies have attempted to clarify the processes that
101 contribute to the generation of SST anomalies in the KOCR, which is a key variable for air–sea
102 interactions (Pak et al., 2017; Qiu, 2000; Qiu & Kelly, 1993; Vivier et al., 2002). Unlike majority
103 of the extratropical ocean, SST variations in the KOCR are predominantly regulated by ocean
104 dynamical process, rather than being passively forced by the atmosphere (Sugimoto & Hanawa,
105 2011; Tanimoto et al., 2003). The dynamical and thermodynamical processes responsible for
106 these SST anomalies are governed by multiple factors, with both deterministic forcing and
107 intrinsic variability contributing to their variations. On the one hand, upwelling/downwelling
108 Rossby waves excited by the large-scale wind stress curl anomalies in the central to eastern part
109 of the North Pacific alter the intensity of the inertial jet, the latitude of the subtropical-subarctic

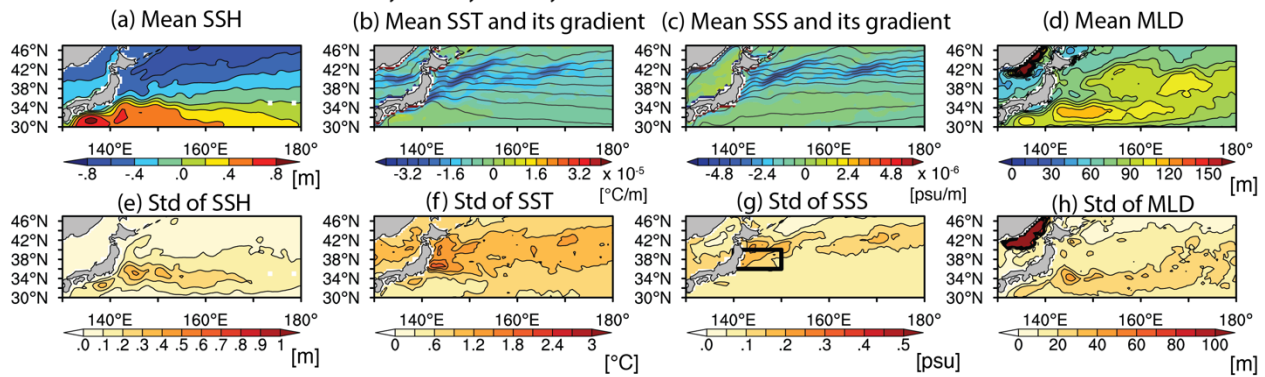
110 gyre, and the thermocline depth of the KOCR, giving rise to significant SST anomalies (Kwon &
111 Deser, 2007; Nonaka et al., 2006, 2008; Schneider et al., 2002; Seager et al., 2001). These
112 changes in large-scale ocean circulation also affect the strength of mesoscale eddy activity (Qiu
113 & Chen, 2005, 2010) and associated heat transport (Itoh & Yasuda, 2010; Sasaki & Minobe,
114 2015; Sugimoto et al., 2014). Furthermore, changes in the Ekman transport associated with
115 anomalous wind forcing may also contribute to the generation SST anomalies (Nakamura &
116 Kazmin, 2003; Yasuda & Hanawa, 1997). In addition to such deterministic forcing, internal
117 variability arising from nonlinearities in the western boundary current system (Pierini, 2006;
118 Pierini et al., 2009; Taguchi et al., 2007) also play an important role in the low-frequency
119 variability of the KOCR, particularly on the frontal scale (Nonaka et al., 2012, 2016, 2020;
120 Taguchi et al., 2007). Superimpositions of these two factors (i.e. external forcing and intrinsic
121 variability) and mutual interactions between them control the observed variability in the KOCR
122 (Qiu & Chen, 2010; Taguchi et al., 2007, 2010).

123 Although our knowledge of the upper ocean dynamics and thermodynamics of the KOCR
124 has been considerably enhanced by a large body of previous literature, less is known about
125 salinity, which also exhibits pronounced low-frequency variation (Fig. 1g). This is attributed to
126 the paucity of in-situ salinity observations and difficulty in accurately simulating salinity in
127 numerical ocean models; however, the deployment of Argo profiling floats in the 2000s have
128 rapidly changed this situation. Newly available datasets based on the Argo profiles have enabled
129 the identification of long-term trends and low-frequency variability in the surface and subsurface
130 salinity in the western North Pacific (Geng et al., 2018; Kitamura et al., 2016; Nan et al., 2015;
131 Yan et al., 2013). The governing mechanisms of such salinity variations have also been explored
132 by means of a salinity budget analysis (Geng et al., 2018; Kitamura et al., 2016; Nagano et al.,

133 2014; Sugimoto et al., 2013), but the relative importance of the freshwater flux and advective
134 processes has not been conclusively established in these studies. Such discrepancies could be due
135 to insufficient spatiotemporal resolutions of the observational and reanalysis products used in
136 these studies; therefore, further quantitative assessments based on more comprehensive
137 observations and/or high-resolution ocean models are required. In addition, the possible impacts
138 of these salinity variations on density structures and the evolution of SST are yet to be assessed,
139 although salinity has been shown to play active roles in the tropical climate variability, such as
140 the El Niño-Southern Oscillation (ENSO) (Hasson et al., 2013; Vialard & Delecluse, 1998; Zhu
141 et al., 2015) and the Indian Ocean Dipole (Kido et al., 2019a, 2019b; Kido & Tozuka, 2017; Li et
142 al., 2018; Zhang et al., 2016). Given that seawater density becomes more dependent on salinity
143 than temperature in lower temperature conditions (Gill, 1982), salinity variations in the KOCR
144 have the potential to affect upper ocean processes and related parameters.

145 To address these issues, we investigate the features and mechanisms of salinity variations
146 in the KOCR through an analysis of the observational datasets and an eddy-resolving ocean
147 reanalysis product. In addition, the potential impacts of salinity upon the mixed layer processes
148 are further examined by means of sensitivity experiments using a one-dimensional mixed layer
149 (1-D ML) model. The remainder of this paper is organized as follows. In Section 2, we outline
150 the observational datasets and ocean reanalysis product used in this study. We also briefly
151 describe the 1-D ML model adopted to assess the salinity impacts. The main features of salinity
152 variations in the KOCR and their underlying mechanisms are discussed in Section 3. Then, in
153 Section 4, we assess the impacts on the density structure and SST through a decomposition of the
154 density anomalies and sensitivity experiments using the 1-D ML model. A summary and
155 discussion are presented in Section 5.

SST, SSS, SSH, and MLD from FORA-WNP30



156

157

158

159

160

161

162

163

164

165

166

167

168

Figure 1. Long-term mean climatology of annual mean: (a) sea surface height (SSH: in m); (b) sea surface temperature (SST: in °C) and its meridional gradient (color); (c) sea surface salinity (SSS: in psu) its meridional gradient (color); and (d) mixed layer depth (MLD in m) derived from the Four-Dimensional Variational Ocean Reanalysis for the Western North Pacific over 30 Years (FORA-WNP30). The contour intervals in (a), (b), (c), and (d) are 0.1, 4×10^{-6} , 6×10^{-7} , and 10, respectively, and the MLD is defined as the depth at which the potential density increases by 0.125 kg m^{-3} from the sea surface. (e)-(h): As in (a)-(d), but with the standard deviation of interannual anomalies (with monthly climatology removed and a 3-month running mean is applied to anomaly fields). Contour intervals in (e), (f), (g), and (h) are 0.1, 0.3, 0.05, and 10, respectively.

169 **2. Data and method**

170 2.1 Observational data

171 In the present study, we analyze the Argo-based gridded temperature and salinity field
172 provided by the Scripps Institution of Oceanography (Roemmich & Gilson, 2009; hereinafter
173 RG09), which has a horizontal resolution of 1° longitude \times 1° latitude and 58 vertical levels, 25
174 of which are in the upper 300 m. Monthly data from January 2004 to December 2019 is used in
175 this study. Prior to the analysis, a linear interpolation for 5-m intervals is applied onto the vertical
176 profiles in temperature and salinity. To check the robustness of results, we also adopted the Grid
177 Point Value of the Monthly Objective Analysis (MOAA-GPV) (Hosoda et al., 2008).

178 To complement the limited spatiotemporal coverage of the Argo data and extend the
179 analysis period to 1990s, we use the Four-Dimensional Variational Ocean Reanalysis for the
180 Western North Pacific over 30 Years (FORA-WNP30). The FORA-WNP30 is an eddy-resolving
181 ocean reanalysis product developed by the Meteorological Research Institute of the Japan
182 Meteorological Agency (MRI-JMA) and the Japan Agency for Marine-Earth Science and
183 Technology (JAMSTEC) (Usui et al., 2017). The core ocean model employed for the FORA-
184 WNP 30 is the MRI Community Ocean model version 2.4 (Tsujino et al., 2006), which is
185 configured for the western North Pacific (117°E to 160°W , 15°N to 60°N). The model has a
186 spatially varying horizontal resolution, with $1/10^\circ$ from 117°E to 160°E (from 15°N to 50°N)
187 and $1/6^\circ$ from 160°E to 160°W (from 50°N to 60°N) in the zonal (meridional) direction, and 54
188 vertical levels, with increasing grid spacing from 1 m at the surface to 600 m at the bottom (set to
189 6300 m depth). Atmospheric forcing of the model is derived from the JRA-55 atmospheric
190 reanalysis product (Kobayashi et al., 2015) with a daily resolution. The FORA-WNP30
191 assimilates various observational data, such as in situ temperature and salinity profiles (including

192 Argo profiles), gridded sea surface height (SSH), SST, and sea ice concentrations derived from
193 satellites using the four-dimensional variational scheme called the MOVE-4DVAR (Usui et al.,
194 2015). In addition to temperature and salinity, we analyze the SSH and horizontal velocity to
195 explore the related physical processes. Surface and subsurface oceanic fields of the FORA-
196 WNP30 have been validated against various types of in-situ and satellite observation (Usui et al.
197 2017) and realistically reproduce the observed seasonal features, such as the location of the
198 ocean fronts (Kida et al., 2015) and the wintertime ML distribution (Suga et al., 2004) in the
199 western North Pacific (for example, see their Fig. 12). As in the MOAA-GPV, all three-
200 dimensional data were linearly interpolated into 5-m intervals in the vertical direction. The
201 FORA-WNP30 data are available for between January 1982 and December 2014 as a daily
202 average, but we focus on the period from 1991 to 2013, as the surface atmospheric flux product
203 employed in this study (J-OFURO3; for a description, see below) is not available for other
204 periods. We note that the results are qualitatively similar even if we use outputs from the entire
205 period.

206 In addition to the gridded Argo data and FORA-WNP30, the surface variables (net heat
207 surface fluxes, including shortwave and longwave radiation, sensible and latent heat fluxes, and
208 freshwater flux) from the Japanese Ocean Flux Datasets with Use of Remote Sensing
209 Observation (J-OFURO3) (Tomita et al., 2019) at a horizontal resolution of 0.25° and available
210 from 1991 to 2013 are employed to examine the possible contribution of atmospheric forcing.

211

212 **2.2 1-D model experiment**

213 To quantitatively assess the potential impact of salinity anomalies on the mixed layer
214 formation and evolution of SST, we need to explicitly deal with the vertical mixing operating

215 within the upper ocean. Given the strong horizontal currents and associated large heat and salt
 216 transports in this region (Qiu & Kelly, 1993; Vivier et al., 2002), here we adopt a 1-D ML model
 217 that can implicitly incorporate advective effects through prescribed forcing (Kido & Tozuka,
 218 2017) and conducted a series of sensitivity experiments. The 1-D ML model employed in this
 219 study is a level-2.5 turbulence closure model that was originally formulated by Furuichi et al.
 220 (2012). The governing equations for temperature (T), salinity (S), and horizontal velocity (u and
 221 v represent zonal and meridional velocity, respectively) in the 1-D ML model are as follows:

$$\frac{\partial T}{\partial t} = \frac{\partial}{\partial z} (\kappa_T \frac{\partial T}{\partial z}) + \frac{1}{\rho_0 C_p} \frac{\partial I}{\partial z} + Res_T(t, z) \quad (1)$$

$$\frac{\partial S}{\partial t} = \frac{\partial}{\partial z} (\kappa_S \frac{\partial S}{\partial z}) + Res_S(t, z) \quad (2)$$

$$\frac{\partial u}{\partial t} = f(v - v_{geo}) + \frac{\partial}{\partial z} (\kappa_V \frac{\partial u}{\partial z}) + Res_u(t, z) \quad (3)$$

$$\frac{\partial v}{\partial t} = -f(u - u_{geo}) + \frac{\partial}{\partial z} (\kappa_V \frac{\partial v}{\partial z}) + Res_v(t, z) \quad (4)$$

222 where ρ_0 ($=1023 \text{ kg m}^{-3}$) is the reference density, C_p ($=3940 \text{ J kg}^{-1} \text{ K}^{-1}$) the specific heat
 223 of the seawater, I the penetrating shortwave radiation, and f the Coriolis parameter. Here, the
 224 shortwave penetration was computed by assuming the Jerlov water type IA (Paulson & Simpson,
 225 1977). κ_T , κ_S , and κ_V denote the vertical diffusion coefficients of heat, salt, and momentum,
 226 respectively, and are internally computed in the model by the turbulence closure scheme, which
 227 is primarily based on the local density stratification (calculated from T and S) and vertical shear
 228 of horizontal currents at each vertical level (see Furuichi et al. (2012) for details). The major
 229 update from Kido & Tozuka (2017) is the implementation of geostrophic velocity (u_{geo} , v_{geo}),
 230 which is externally added to the model as the boundary condition. This modification is essential
 231 for the better simulation of velocity fields in the midlatitude ocean, particularly over regions with
 232 swift currents. The last term in each equation, namely $Res_T(t, z)$, $Res_S(t, z)$, $Res_u(t, z)$, and

233 $Res_v(t, z)$, are referred to as the dynamical correction term, and it represents a contribution from
234 the three-dimensional processes (e.g., horizontal and vertical advection), which cannot be
235 explicitly treated in the 1-D framework. These terms are estimated on the basis of the specified
236 temperature, salinity, and horizontal velocity as described below using technique proposed in
237 Kido & Tozuka (2017). To summarize, the external forcing components necessary for
238 conducting the model experiment are surface atmospheric forcing (heat, freshwater, and
239 momentum fluxes), geostrophic current fields, and three-dimensional oceanic variables used for
240 the initializations and computations of the dynamical corrections. Such implicit incorporations of
241 advective effects into the 1-D ML model have also been adopted in other studies (Vivier et al.,
242 2002), and shown to realistically serve as a substitute for the 3-D dynamical processes. For more
243 comprehensive descriptions of our 1-D ML model, interested readers are referred to Furuichi et
244 al. (2012) and Kido & Tozuka (2017).

245 In this study, the 1-D ML is configured at each grid point over a domain covering the
246 western North Pacific region (135° – 170° E, 30° N– 50° N) with 0.5° longitude \times 0.5° latitude. The
247 model has a variable vertical resolution, from 2 m near the surface to 10 m at the bottom (the
248 maximum depth is set to 1000 m). Daily shortwave/longwave radiation, 10 m winds, air
249 temperature, specific humidity, and monthly precipitation from J-OFURO3 (Tomita et al., 2019)
250 are used to force the model. Turbulent heat flux, evaporation, and wind stress are calculated
251 using the bulk formulae of Kara et al. (2005). Geostrophic currents are calculated using the
252 density field of the FORA-WNP30, assuming a level of no motion at 2000 m. Initial and
253 restoring conditions (three-dimensional profiles of temperature, salinity, and horizontal current)
254 are then taken from the FORA-WNP30.

255 Using atmospheric and oceanic forcing as outlined above, we first conducted a
256 preliminary experiment to obtain the dynamical correction terms necessary for the realistic
257 simulation of oceanic variability in the KOCR. For this experiment, the model was initialized
258 from October 15 of each year from 1991 to 2012 and then integrated forward for 12 months with
259 atmospheric forcing and geostrophic currents, while restoring the modeled temperature, salinity,
260 and horizontal velocity toward the values derived from the FORA-WNP30 with a nudging time
261 scale of 5 days. During the integration of this experiment, the dynamical correction terms (e.g.,
262 $\frac{T_{FORA}-T}{5 [days]}$ in the case of temperature, where T_{FORA} denotes the temperature value of the FORA-
263 WNP30) were computed at each time step and stored as 1-day averaged values for use in the
264 subsequent experiments. These dynamical corrections were essential for realistically constraining
265 the time evolution of the temperature and horizontal velocity in the subsequent sensitivity
266 experiments. Next, we performed the control (CTL) experiments, for which the model was
267 initialized and integrated with the same atmospheric and oceanic conditions with those in the
268 preliminary experiment, but the nudging of the temperature and horizontal velocity was turned
269 off and the dynamical correction terms obtained from the preliminary integrations were used
270 instead (note that salinity was still relaxed to the FORA-WNP30's value with the nudging time
271 scale of 5 days). As in the preliminary experiment, the CTL experiment was also conducted for
272 all years from 1991 to 2013 in order to simulate the observed variations in the KOCR. As the
273 dynamical correction terms were archived with a high temporal resolution (1-day averaged
274 values were used), the temperature, salinity, and current fields from the CTL experiment were
275 very similar to, or nearly identical, to those from the preliminary experiment (figures not shown).
276 This experiment was used as a reference for comparison to the sensitivity experiment described
277 in Section 4.2.

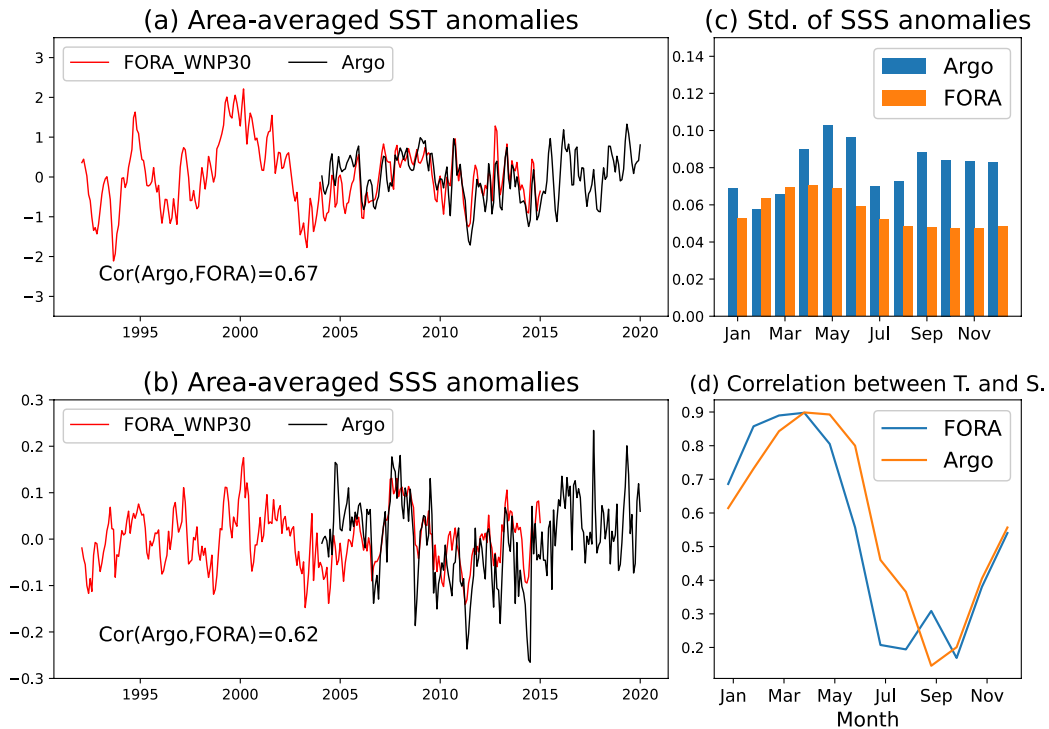
278 **3. Features of salinity variation in the KOCR**

279 **3.1 Features**

280 First, we examine the time series of temperature and salinity anomalies averaged over the
281 KOCR (142°–153°E, 36°–40°N; see the inset black box in Fig. 1g) obtained from the Argo
282 product and FORA-WNP30 (Figs. 2a, b). Note that this box is chosen to adequately cover the
283 transition region between the Kuroshio Extension (KE) and the Subarctic Front (Kida et al.,
284 2015). Over the KOCR, SST and SSS anomalies exhibit coherent interannual to decadal
285 fluctuations, and their time evolution in the Argo product agree well with those in the FORA-
286 WNP30. Indeed, the temporal correlation coefficient between the Argo product and FORA-
287 WNP30 was 0.67 for SST and 0.62 for SSS, both of which were statistically significant at a 90%
288 confidence level based on the bootstrap method (here, we have generated 10,000 randomly
289 ordered data and estimated the confidence intervals of the correlation coefficients). The spatial
290 patterns of climatological surface and subsurface temperature and salinity over the KOCR also
291 agreed well between the Argo and FORA-WNP30 (figures not shown). For these reasons, we
292 conclude that the FORA-WNP30 adequately reproduced the observed oceanic variability in this
293 region. More thorough validations of the FORA-WNP30 against various observational data are
294 presented by Usui et al. (2017).

295 To delineate the seasonality of salinity variation, the standard deviation of interannual
296 variability of area-averaged SSS anomalies over the KOCR and their correlation coefficient with
297 SST anomalies over the same region were calculated for each calendar month (Figs. 2c, d). In
298 both the Argo and reanalysis products, the peak of the SSS variation was found to be around the
299 boreal spring, although the FORA-WNP30 slightly underestimated the observed amplitude (Fig.
300 2c). The coherence between the temperature and salinity was also strong during this season (Fig.

301 2d), while it was relatively weak during the summer and fall. Considering this seasonality of SSS
 302 variability and annual cycle of MLD, in the analysis that follows, we will primarily focus on the
 303 salinity variation during the late winter to boreal spring (February-April averaged values).
 304



305
 306 Figure 2. (a) Time series of 3-month averaged SST and (b) SSS anomalies averaged
 307 over the KOCR (142°E-153°E, 36°N-40°N; see black box in Fig. 1g) from the Argo
 308 product (black) and FORA-WNP30 (red). Note that anomalies of the Argo product
 309 (FORA-WNP30) are relative to their seasonal mean values from 2004 to 2019
 310 (1991 to 2013). The correlation coefficients between the Argo product and FORA-
 311 WNP30 are shown in the lower left. (c) Standard deviation of the SSS anomalies
 312 averaged over the KOCR as a function of calendar months from the Argo product
 313 (orange) and FORA-WNP30 (blue). (d) As in (c), but for correlation coefficients

314 between SST and SSS anomalies over the KOCR. The unit for SST (SSS) is °C
 315 (psu).

316
 317 As can be seen in the time series of SST and SSS anomalies (Figs. 2a, b) and their
 318 correlation (Fig. 2d), anomalous saltening (freshening) in the KOCR tends to co-occur with
 319 warming (cooling) therein. To objectively detect such anomalous events and extract features
 320 common to all cases, we will define positive and negative years as follows: a positive (negative)
 321 year is defined as one with both February to April averaged SST and SSS anomalies over the
 322 KOCR that are larger (smaller) than their 0.5 standard deviation. According to this criterion, 6
 323 (8) positive years and 4 (6) negative years can be identified in the Argo data (FORA-WNP30)
 324 (Table 1).

325

	Positive years	Negative years
Argo (RG09)	2007, 2008, 2009, 2013, 2016, 2019 (6 events)	2011, 2012, 2014, 2015 (4 events)
Reanalysis (FORA- WNP30)	1997, 1999, 2000, 2002, 2007, 2008, 2009, 2013 (8 events)	1996, 2003, 2004, 2005, 2010, 2011 (6 events)

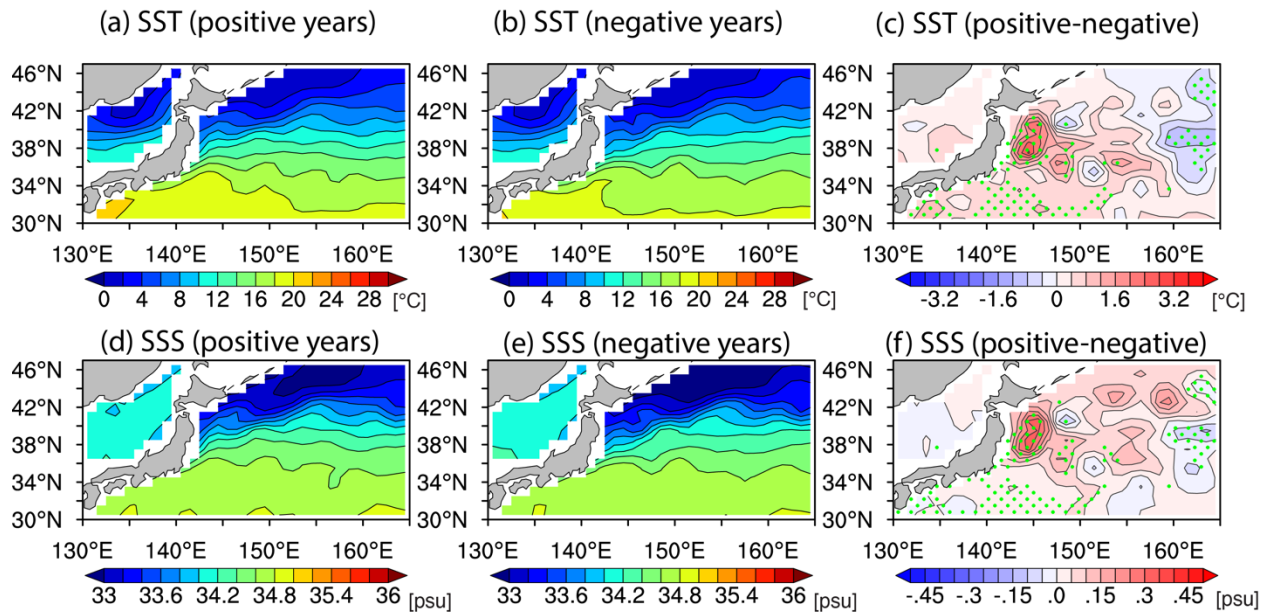
326 Table 1. Positive and negative years identified in the Argo data (RG09) and
 327 reanalysis product (FORA-WNP30).

328

329 Composites of the temperature and salinity field during the mature phase of positive and
330 negative years (averaged for February-April) obtained from the Argo product are shown in Fig. 3.
331 We note here that the features in the composites with January–March mean are qualitatively
332 similar to the following composites. During positive years, warm and saline water from the
333 subtropical region extends farther to the north compared to negative ones (Figs. 3a, b, d, e). As
334 expected from the definition of events, regions with significant differences in SST tend to be
335 collocated with those in SSS (Figs. 3c, f). Similar patterns are also found in composites from the
336 FORA-WNP30 (Fig. 4), although small-scale features are more evident and the amplitude of
337 SSS anomalies is slightly smaller than that in the Argo data. As the gross features of composite
338 fields constructed from the Argo data of the overlapping period (2004-2013) were very similar to
339 the original ones (figures not shown), quantitative differences between the Argo and FORA-
340 WNP30 may be caused by those in their horizontal resolution and analysis method, rather than
341 the analysis period. Such anomalous warming events in the KOCR have also been noted in
342 several previous studies (Masunaga et al., 2016; Qiu et al., 2017; Sugimoto et al., 2014);
343 however, these studies have not specifically focused on associated salinity variations. These
344 studies have pointed out that the low-frequency fluctuations of SST over the KOCR are related
345 to the modulation of dynamic states of the KE. To determine whether such arguments also apply
346 to our selected positive/negative years, we will explore the origin of these temperature and
347 salinity variations in the next subsection.

348

Composite of SST and SSS from Argo

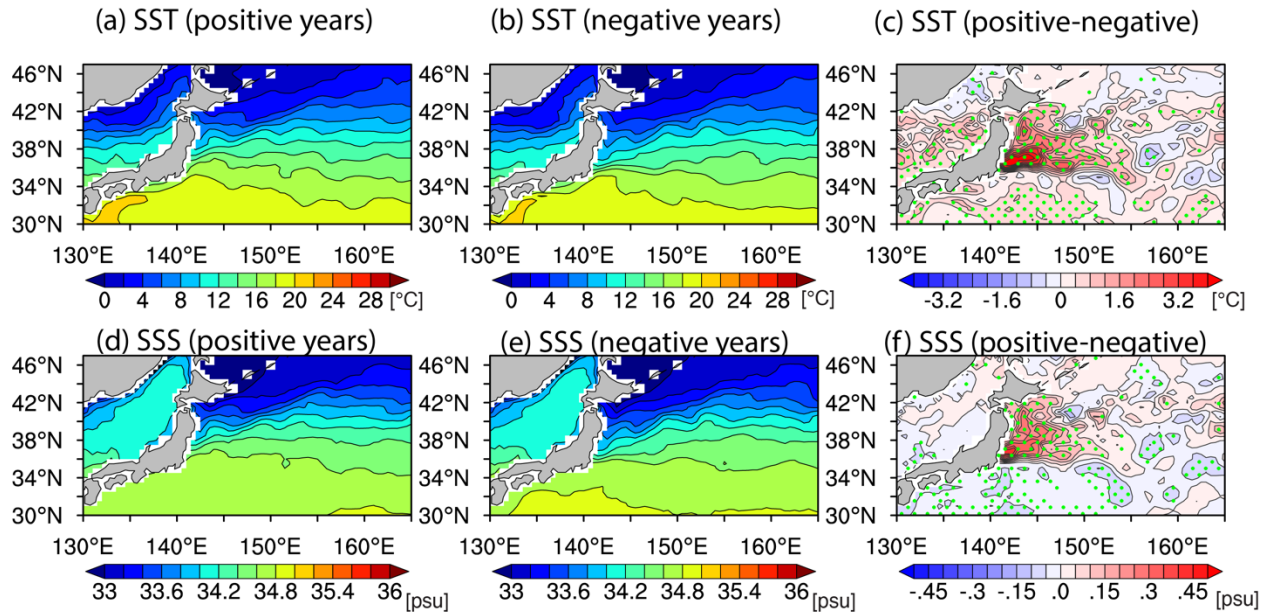


349

350 Figure 3. (a)-(c): Composite of SST fields (in °C) during February-April of (a)
 351 positive and (b) negative years from the Argo data. Differences between positive
 352 and negative years (i.e. (a) minus (b)) are shown in (c). The contour intervals in (a)
 353 and (b) are 2, whereas those in (c) are 0.4. Differences that are significant at the
 354 80% confidence levels based on a two-tailed t-test are green dotted in (c). (d)-(f):
 355 As in (a)(c), but for SSS fields (in psu). The contour intervals in (d) and (e) are 0.2,
 356 whereas those in (f) are 0.05.

357

Composite of SST and SSS from FORA-WNP30



358

359 Figure 4. As in Fig. 3, but from the FORA-WNP30.

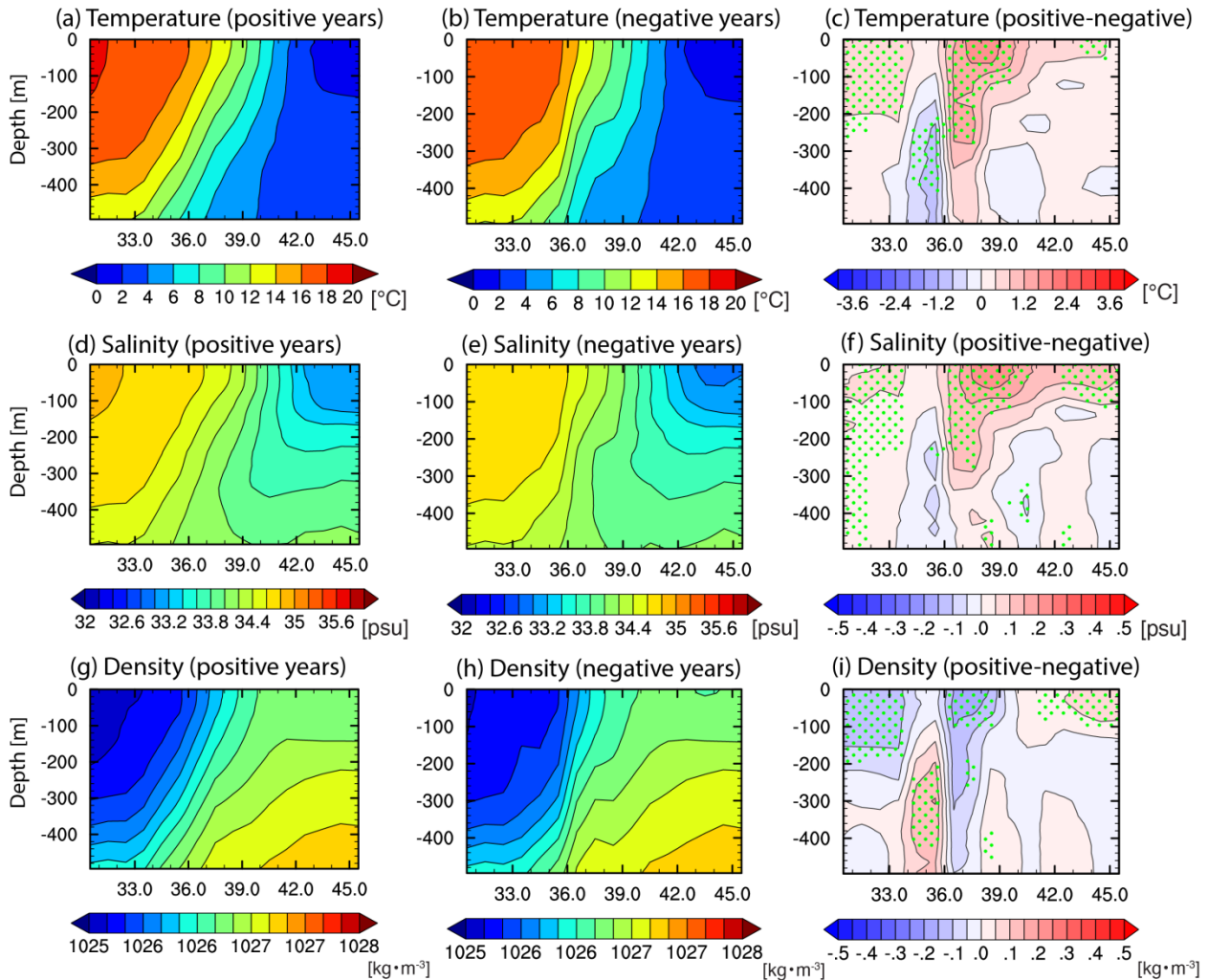
360

361 To examine the driving mechanisms of temperature and salinity variations over the
 362 KOCR, it is helpful to emphasize their vertical structure. For this purpose, latitude-depth sections
 363 of zonally averaged (142°–153°E) composited temperature, salinity, and potential density from
 364 the Argo data are depicted in Fig. 5. For both positive and negative years, prominent density-
 365 compensating temperature and salinity fronts are seen around 36°–39°N and they extend to the
 366 upper 200 m (Figs. 5a, b, d, e). Comparison of the temperature and salinity fields between the
 367 positive and negative years reveals that strong warming and saltening is observed in the KOCR
 368 during the positive years, while the opposite is observed in the negative years (Figs. 5c, f). Large
 369 differences in temperature and salinity are found near the surface to the north of 38°N (i.e., the
 370 subarctic region), whereas they are found near the thermocline depth (from 200 to 400 m depth)

371 to the south (Figs. 5c, f). Such latitudinal differences in the vertical structures of low-frequency
372 thermohaline anomalies have also been noted by Nonaka et al. (2006).

373 Interestingly, the differences in potential density are characterized by meridional dipole
374 structures (Fig. 5i) with negative anomalies (i.e., a decrease in density) to the south and positive
375 anomalies to the north. The causes of these density anomalies will be discussed in the next
376 section by decomposing these anomalies into respective contributions from temperature and
377 salinity. Similar patterns of temperature, salinity, and potential density anomalies are also
378 observed in composited fields obtained from the FORA-WNP30, although anomalies over the
379 northern part are slightly underestimated (Fig. 6). Hence, we believe that the differences in the
380 upper ocean fields between the positive and negative years are robust features across the datasets
381 and analysis periods. In the next subsection, we will explore the governing mechanisms of these
382 events and possible links to large-scale variability by inspecting the features of other variables.
383

Composite of temperature, salinity, and density from Argo



384

385

386

387

388

389

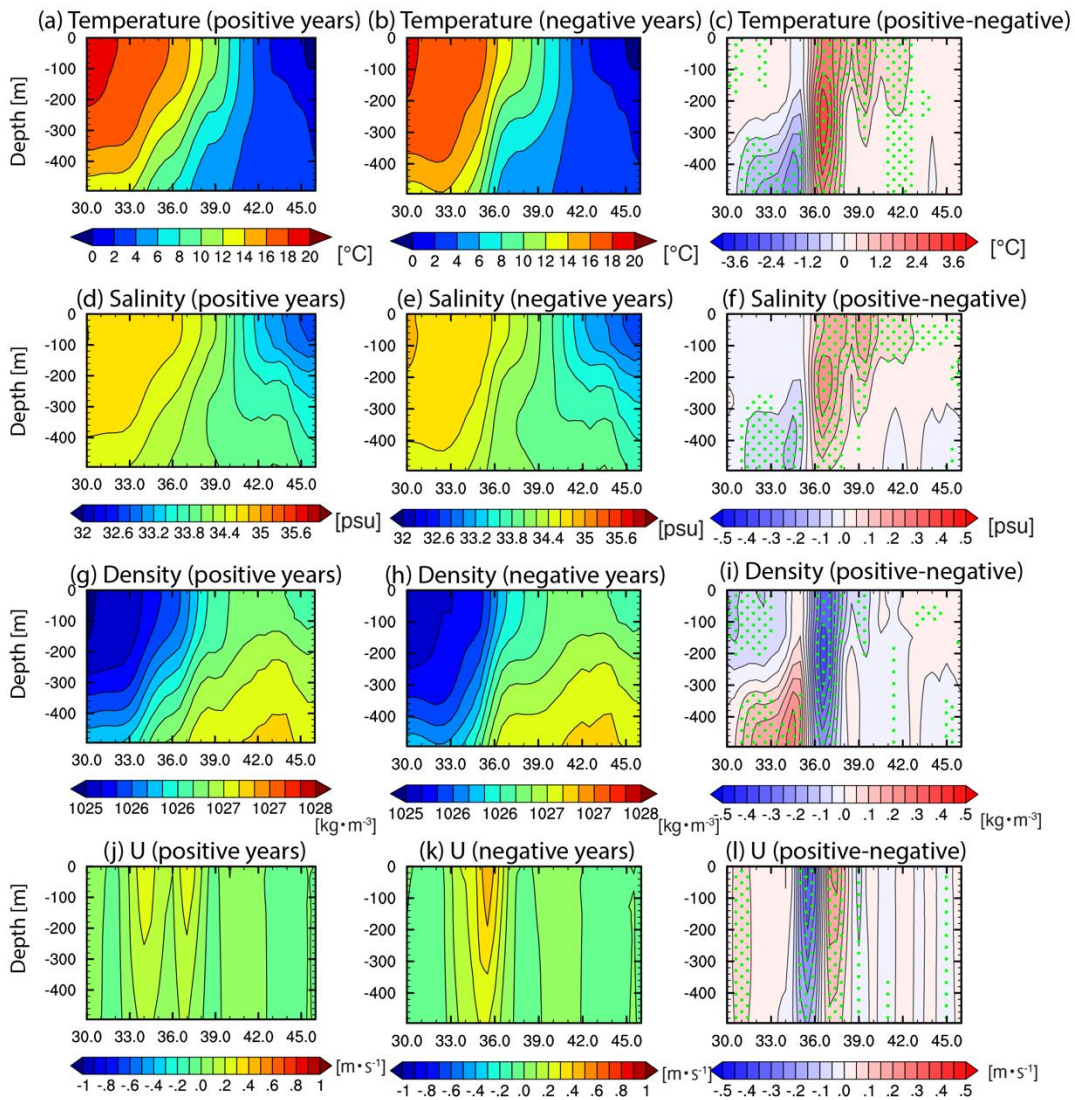
390

391

Figure 5. (a)-(c): Latitude-depth section (zonally averaged from 142°-153°E) of composited temperature (in °C) fields during February-April of (a) positive and (b) negative years, and (c) their differences from the Argo data. The contour intervals are 2 in (a) and (b), whereas those in (c) are 0.4. Differences that are significant at the 80% confidence levels based on a two-tailed t-test are green dotted in (c). (d)-(f): As in (a)-(c), but for salinity fields (in psu). The contour intervals are 0.2 in (d) and (e), and those in (f) are 0.05. (g)-(i): As in (a)-(c), but for potential density

392 fields (in kg m^{-3}). The contour intervals are 0.2 in (g) and (h), whereas those in (i)
 393 are 0.05.
 394

Composite of temperature, salinity, density, and zonal velocity from FORA-WNP30



395
 396 Figure 6. (a)-(i): As in Fig. 5, but from the FORA-WNP30. (j)-(l): As in (a)-(c), but
 397 for the zonal current fields (in m s^{-1}). The contour intervals in (j) and (k) are 0.1
 398 and 0.05 in (l).

399 **3.2 Mechanisms**

400 There are several candidates that induce co-variations in temperature and salinity
401 variations over the KOCR. First, changes in the local atmospheric conditions, such as anomalous
402 heat and freshwater exchanges at the sea surface can directly generate in-phase and/or out-of-
403 phase variations in SST and SSS. Second, an anomalous strengthening or weakening of large-
404 scale ocean circulation (both the Ekman and geostrophic current) may modulate temperature and
405 salinity advection, thereby creating significant anomalies. Third, a modulation in the strength of
406 the mesoscale eddy activities affects the magnitude of the eddy-induced transport of heat and
407 freshwater transport, thereby leading to significant temperature and salinity anomalies. To
408 identify relative contribution from these factors and underlying physical processes, composites of
409 various physical parameters are presented in Figure 7. Because the growing season of
410 temperature and salinity anomalies in the KOCR is a few months prior to the mature phase (the
411 lead-lag relationship between the SSS anomalies and SSS tendency anomalies is shown in Fig.
412 8), we focus on differences averaged from December to February.

413 Due to the outbreak of cold and dry air masses from the continent by the westerly wind,
414 the net surface heat flux is mostly upward (i.e., the ocean releases heat into the atmosphere) over
415 the western North Pacific (Figs. 7a, b). Differences between the positive and negative years (Fig.
416 7c) show that the ocean is more strongly cooled by the atmosphere during the positive years in
417 the KOCR. A detailed decomposition of the heat flux anomalies into individual components (i.e.,
418 shortwave and longwave radiation as well as sensible and latent heat fluxes) reveals that warmer
419 SST during the positive years (Fig. 3c) and associated increases in the turbulent heat fluxes are
420 responsible for the total differences (figures not shown). Therefore, the heat flux anomalies serve
421 to dampen the SST anomalies and do not contribute to their generation and growth. These results

422 are in line with those from previous observational studies, which underlined the importance of
423 SST anomalies over the Kuroshio and Oyashio extension regions in driving heat flux variability
424 there (Masunaga et al., 2016; Sugimoto & Hanawa, 2011; Tanimoto et al., 2003).

425 Consistent with the heat flux fields and their interpretation described above, more (less)
426 freshwater is lost to the atmosphere over the KOCR during the positive (negative) years (Figs.
427 7d–f). This is conducive to surface saltening (freshening) in the positive (negative) years and
428 could contribute to the generation of the observed SSS anomalies. Unsurprisingly, these
429 differences in freshwater fluxes are primarily due to changes in evaporation, while no significant
430 differences were found in the precipitation fields. The maximum amplitude of freshwater flux
431 differences is approximately $2 \times 10^{-8} \text{ m s}^{-1}$, which leads to changes in the mixed layer salinity of
432 0.02 psu per month, assuming the mixed layer depth of 100 m. This value is rather smaller than
433 the observed total SSS differences (~ 0.2 psu) and could explain only one–third of the anomaly in
434 three months, suggesting that other processes, such as anomalous salinity advection, may also be
435 important for the generation of salinity variations.

436 To highlight the roles played by oceanic processes, we next compare low-passed sea
437 surface height, surface current, and eddy kinetic energy (EKE) fields between positive and
438 negative years (Figs. 7g–l). Here, the low-frequency (high-frequency) signals were obtained by
439 applying a 300-day (Qiu & Chen, 2005) Lanczos low-pass (high-pass) filter (Duchon, 1979) to
440 the total fields.

441 Differences in the SSH fields between the positive and negative years are characterized
442 by a meridional dipole over the KE, with the higher (lower) SSH anomalies to the north (south)
443 of the climatological eastward jet (Fig. 7i). More specifically, the signatures of the southern and
444 northern recirculation gyres (Qiu et al., 2008) are markedly discernable and the KE jet is zonally

445 oriented during negative years (Fig. 7h), whereas the KE jet is weaker and convoluted during
446 positive ones (Fig. 7g). These features are suggestive of their link with the bimodal states of the
447 KE (Qiu & Chen, 2005, 2010; Taguchi et al., 2010); a positive (negative) year with weaker
448 recirculation gyres corresponding to an unstable (stable) state of the KE, as speculated in several
449 previous studies (Masunaga et al., 2016; Qiu et al., 2017; Sugimoto et al., 2014). The differences
450 in velocity fields (figures not shown) are nearly in geostrophic balance with those in SSH,
451 suggesting that current anomalies mostly come from the geostrophic components rather than the
452 Ekman current. During positive years, northeastward currents over the KOCR are more
453 prominent than negative years, especially in the southwestern area (36°N – 38°N ; see also Figs.
454 6g–l). The stronger (weaker) northeastward current during positive (negative) years leads to an
455 increase (a decrease) in the advection of warm and salty water from the south, contributing to an
456 anomalous warming and saltening (cooling and freshening) over the KOCR. Such a modulation
457 of advective processes efficiently operates in the climatological frontal regions with strong
458 temperature and salinity gradients and may partly explain the differences in the peak depth of
459 anomalies between the northern and southern areas of the KOCR (Nonaka et al., 2006). The
460 region with significant current anomalies collocates with upstream portions of the quasi-
461 stationary jet (QSJ, also referred to as the J-1) (Isoguchi et al., 2006; Wagawa et al., 2014),
462 which is a conveyor of warm and saline water from the KE to subarctic regions. Thus, these
463 current anomalies may be viewed as a modulation of the QSJ associated with changes in the
464 dynamical state of the KE, as suggested in an observational study by Wagawa et al. (2014).

465 In relation to changes in large-scale ocean circulation, the strength of mesoscale eddy
466 activity undergoes significant variations due to changes in barotropic/baroclinic instability as
467 well as those in the interaction with bottom topography (Qiu & Chen, 2005, 2010; Yang et al.,

468 2017). With respect to the KE, the EKE in the upstream regions substantially decreases when it
469 is in a stable state; conversely, the EKE increases when the KE is in an unstable state. (Itoh &
470 Yasuda, 2010; Qiu & Chen, 2005, 2010; Sasaki & Minobe, 2015; Sugimoto et al., 2014; Taguchi
471 et al., 2010). To confirm consistency with these previous findings, we calculated the EKE as
472 follows:

$$EKE = \frac{1}{2}(u'^2 + v'^2),$$

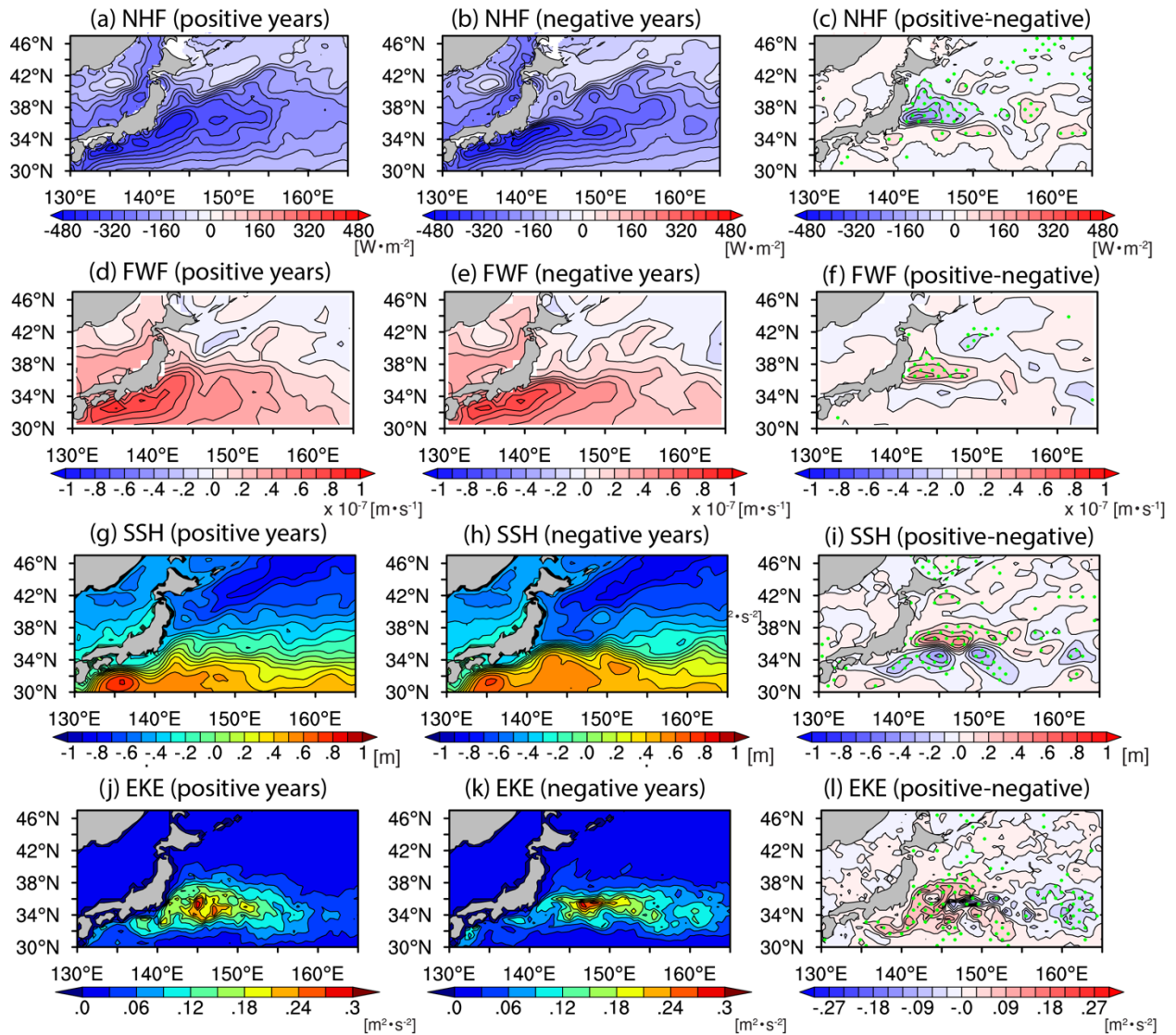
5)

473 where (u', v') denotes high-passed horizontal velocity.

474 During positive years, an elevated EKE level is seen during positive years compared to
475 negative years (Figs. 7j–l), supporting our argument that the positive (negative) years correspond
476 to an unstable (stable) and high eddy-activity state of the KE. As individual mesoscale eddies
477 serve to relax the meridional gradients of temperature and salinity through Lagrangian transports
478 of heat and salt (Dong et al., 2017; Itoh & Yasuda, 2010), the increase (decrease) in numbers and
479 strength of mesoscale eddies during the positive (negative) years is conducive for warming and
480 saltening (cooling and freshening) over the KOCR (Qiu et al., 2017; Sasaki & Minobe, 2015;
481 Sugimoto et al., 2014), as well as anomalous large-scale ocean circulation.

482

Composite of NHF, FWF, SSH, current, and EKE (from J-ORUFO3 & FORA-WNP30)



483

484 Figure 7: (a)-(c): Composite of net surface heat flux (in $W m^{-2}$) during December-
 485 February of (a) positive and (b) negative years, and (c) their differences from the
 486 J-OFURO3. The contour intervals are 50. Here, positive values indicate heating of
 487 the ocean by the atmosphere. Differences that are significant at the 80%
 488 confidence levels based on a two-tailed t-test are green dotted in (c). (d)-(f): As in
 489 (a)-(c), but for net surface freshwater flux (evaporation minus precipitation) (in m

490 s^{-1}). The contour intervals are 1×10^{-8} . (g)-(h): As in (a)-(c), but low-passed sea
491 surface height (in m). The contour intervals are 0.1. (j)-(l): As in (a)-(c), but for the
492 surface eddy kinetic energy (EKE: in $m^2 s^{-2}$). The contour intervals are 0.03.

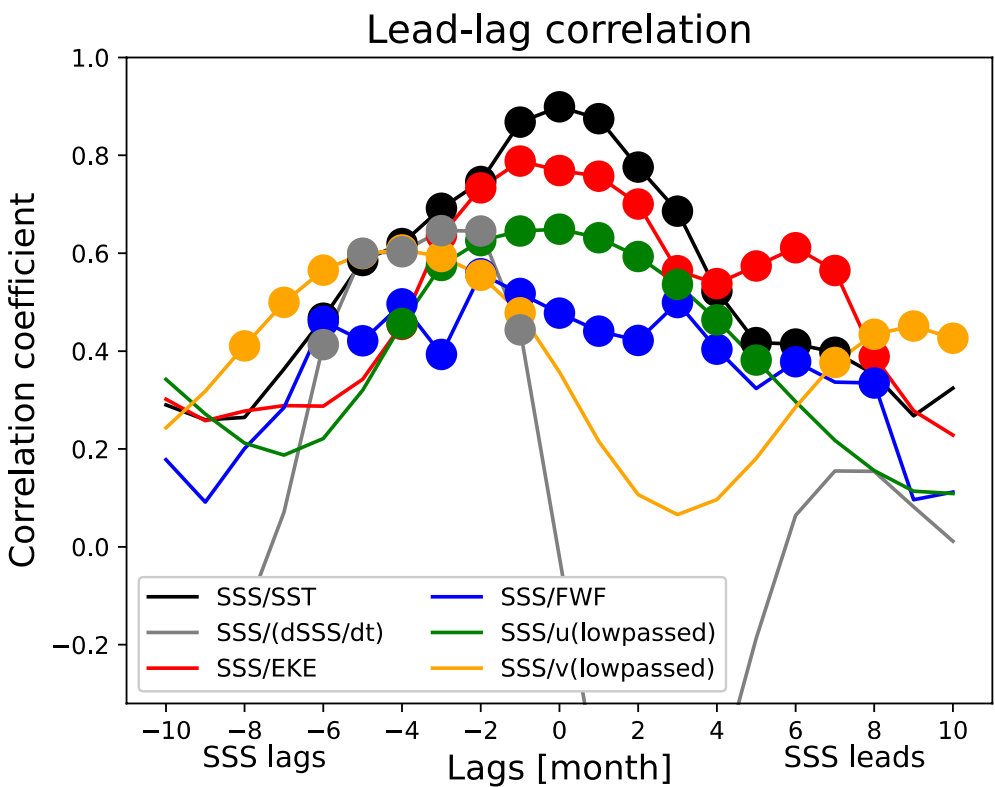
493

494 To confirm the importance of the various processes described above, lead-lag correlation
495 coefficients between February-April mean SSS anomalies over the KOCR and other variables
496 are presented in Fig. 8. As mentioned in Section 3.1 (Fig. 2d), SSS anomalies are highly
497 correlated with SST anomalies over the same region, with its maximum value around lag 0 (Fig.
498 8, black curve). The SSS tendency (i.e., the time derivative of SSS) has a significant positive
499 correlation with SSS anomalies when the former lead the latter by around 2 to 6 months,
500 suggesting that the maximum growth of SSS anomalies occurs a few months before their peak
501 season (grey curve). The freshwater flux anomalies (note that they are defined as evaporation
502 minus precipitation, so that the positive values correspond to increases in SSS) also exhibit
503 significant correlations, but their coefficients are relatively low (~ 0.4), when they lead the SSS
504 anomalies (blue curve). Similar features with a reversed sign were also found for the net heat
505 flux anomalies (figure not shown). Therefore, the local atmospheric anomalies are not the main
506 driver of the observed temperature and salinity variations, although they may play a secondary
507 role in determining their amplitude.

508 For ocean dynamical variables, both zonal and meridional low-pass filtered velocity
509 (orange and green curves) and EKE anomalies are significantly correlated with SSS with leading
510 SSS anomalies, supporting the idea that the temperature and salinity variations over the KOCR
511 are closely linked to the dynamical state of the KE. As the ocean background circulations and
512 mesoscale eddy fields mutually affect each other via eddy-mean flow interaction (Qiu & Chen,

513 2010; Taguchi et al., 2010), it is not straightforward to clearly isolate individual contributions
 514 from both factors. Therefore, herein we qualitatively conclude that changes in the stability of the
 515 KE path leads to coherent changes in the upper ocean temperature and salinity over the KOOCR
 516 through modulation of heat and salt transport by large-scale geostrophic current and mesoscale
 517 eddies, whereas contributions from freshwater flux and Ekman advection anomalies seemed to
 518 be not so important. A comparison of advective terms estimated from the current fields and
 519 salinity of the FORA-WNP30 also corroborated the above conclusion (Fig. S1). For a more
 520 quantitative and comprehensive assessments of these processes, a closed salinity budget analysis
 521 based on a realistic high-resolution ocean model is desirable and could be an interesting topic for
 522 future studies.

523



524

525 Figure 8. Lead-lag correlation coefficients between February-April averaged SSS
526 anomalies over the KOCR and other variables (black: SST; grey: SSS tendency;
527 red: EKE; blue: freshwater flux; green: low-passed surface zonal velocity; and
528 orange: low-passed surface meridional velocity). All oceanic variables (SSS, SST,
529 EKE, surface velocity) are taken from the FORA-WNP30 reanalysis, whereas the
530 J-OFURO3 product is adopted for the freshwater flux. The lag is in units of the
531 month, and positive (negative) values indicate SSS anomaly leads (lags). Correlation
532 coefficients that are significant at the 90% confidence levels on the basis of the
533 bootstrap method are represented by the colored dots.

534 4. Impact of salinity variation

535 In this section, we assess how these salinity variations can alter the upper ocean's
536 hydrographic properties and eventually affect the evolution of the SST, which is a key variable
537 for midlatitude air–sea interaction.

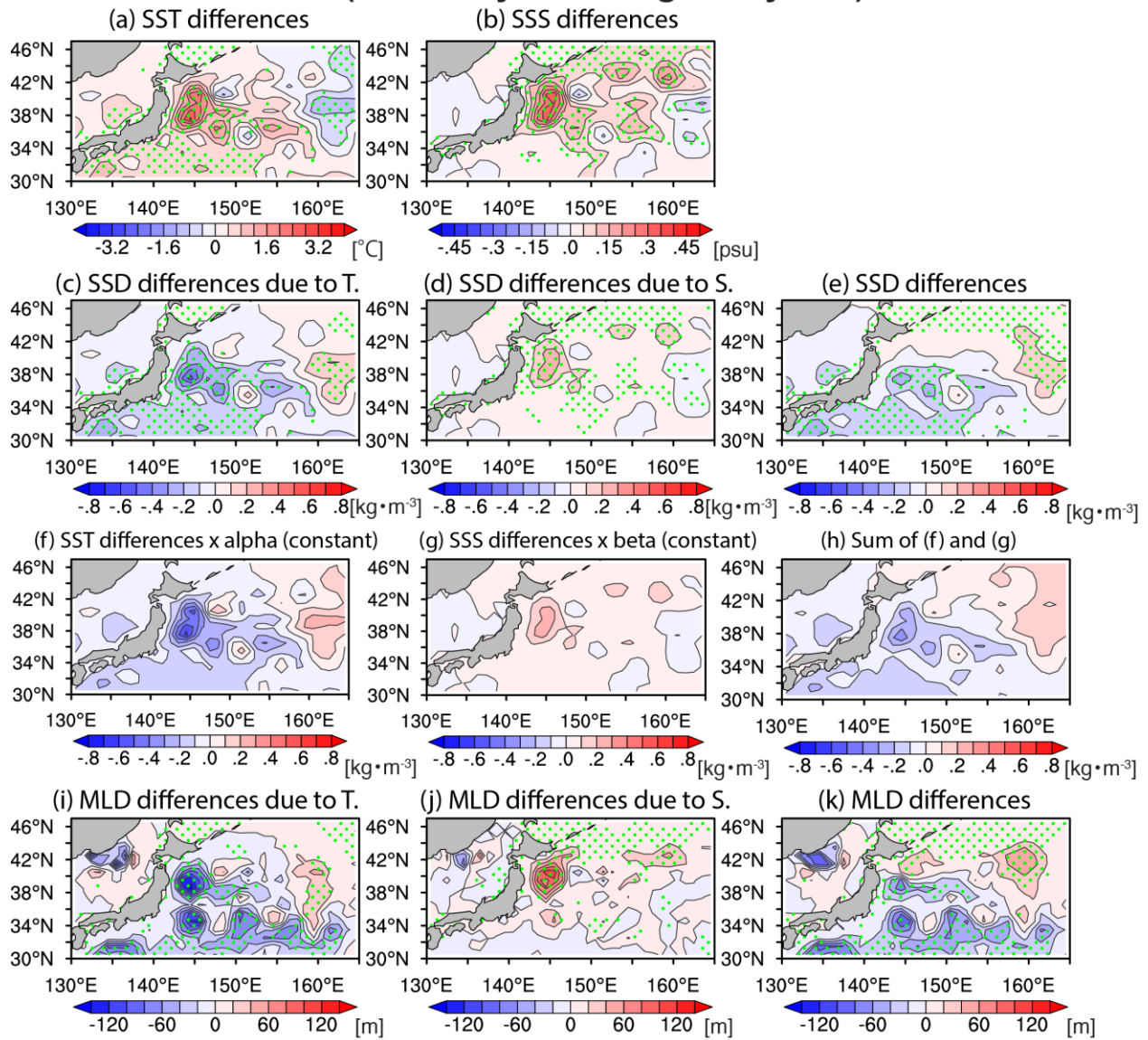
538

539 4.1 Temperature and salinity contributions to density anomalies

540 We calculate the potential density of seawater (denoted as $\rho(T, S)$) using original (i.e.
541 interannually varying) temperature and salinity based on the equation of state by Jackett
542 & McDougall (1995). Then, we compute the potential density using original temperature and
543 climatological salinity (represented by \bar{S}), $\rho_T = \rho(T, \bar{S})$, to isolate the effect of salinity variations.
544 Differences in potential density between the positive and negative years, $\Delta\rho = \rho_{POS}(T, S) -$
545 $\rho_{NEG}(T, S)$, contain both contributions from temperature and salinity differences. For ρ_T ,
546 $\Delta\rho_T = \rho_{POS}(T, \bar{S}) - \rho_{NEG}(T, \bar{S})$ are caused only by the temperature difference. Thus, the
547 contribution from salinity variations to potential density ($= \Delta\rho_S$) can be estimated by considering
548 the differences between $\Delta\rho$ and $\Delta\rho_T$, i.e. $\Delta\rho_S = \Delta\rho - \Delta\rho_T = \{\rho_{POS}(T, S) - \rho_{POS}(T, \bar{S})\} -$
549 $\{\rho_{NEG}(T, S) - \rho_{NEG}(T, \bar{S})\}$. Although the nonlinearity of the equation of state does not allow a
550 complete separation of the density signals into temperature and salinity contributions, this
551 method is useful for illustrating the importance of salinity variations. Differences in other
552 density-dependent variables, such as the buoyancy frequency and mixed layer (see below for
553 detailed definitions) can, in the same manner, be decomposed into temperature and salinity
554 contributions. This approach has been widely used for assessments of salinity impacts over the
555 tropical Pacific (Zheng & Zhang, 2012, 2015) and tropical Indian Ocean (Kido & Tozuka, 2017).

556 The positive temperature and salinity anomalies in the KOCR in the positive years (Figs.
557 9a, b; see also Figs. 3c, f) serve compensate each other in forming anomalous densities, with
558 positive temperature anomalies leading to a decrease in sea surface density (SSD) (Fig. 9c),
559 whereas positive salinity anomalies contribute to increases in the SSD there (Fig. 9d). As a result,
560 negative values of the total SSD differences are confined to the southern part of the KOCR
561 (south of 38°N; Fig. 9e). Similar features are also evident in composites from the FORA-WNP30,
562 although surface saltening and associated compensations of the temperature-related SSD signals
563 are weaker than those in the Argo data (Figs. 10a–e).

Composite differences of SST, SSS, SSD, and MLD from Argo (Positive years - negative years)



564

565 Figure 9. (a), (b): Differences in composited (a) SST (in $^{\circ}\text{C}$) and (b) SSS (in psu)

566 fields between positive and negative year during February-April. The contour

567 intervals in (a) are 0.4, whereas those in (b) are 0.05. (c)-(e) As in (a) and (b), but

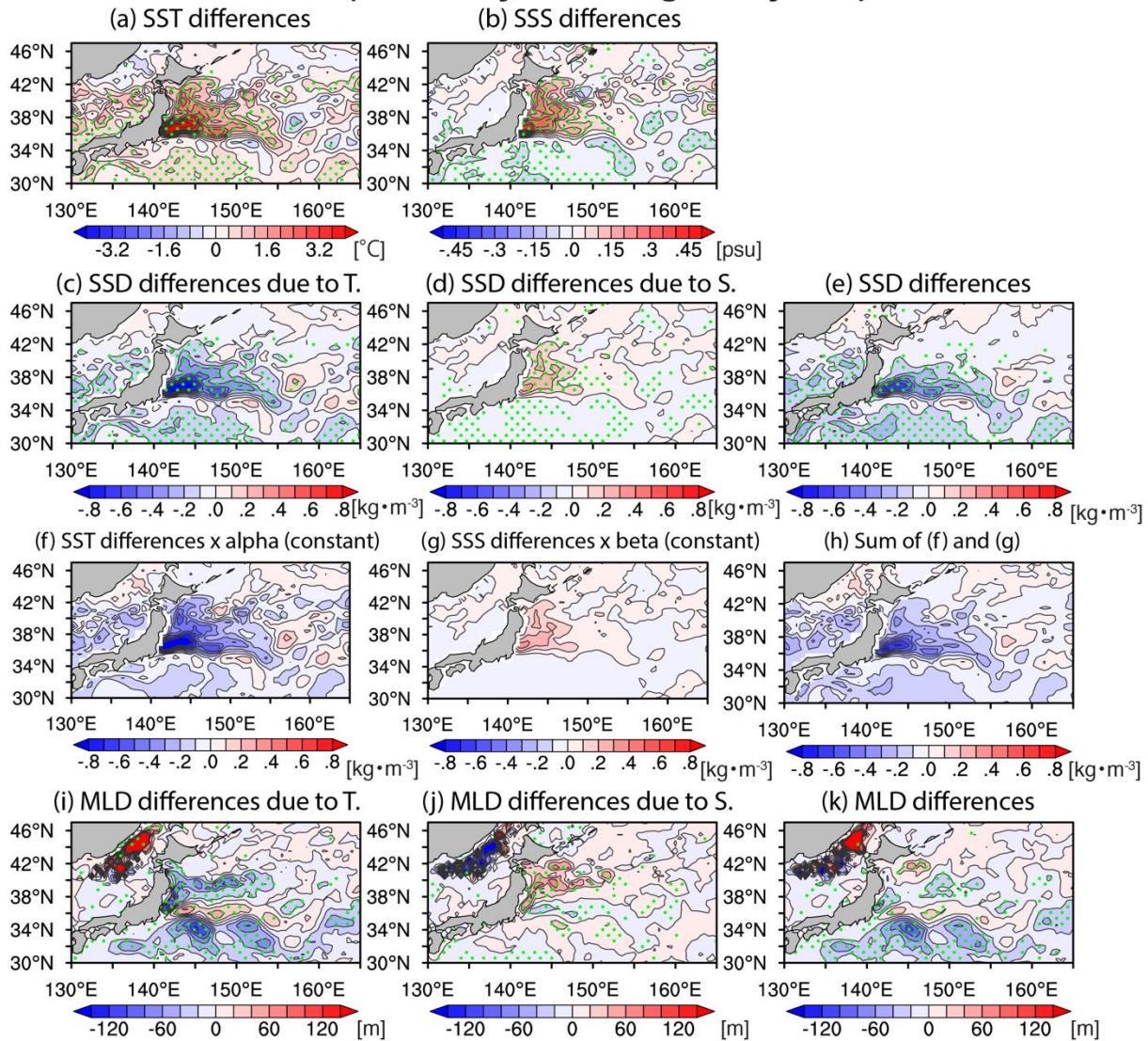
568 for (e) shows the surface density differences and contribution from (c) SST and

569 (d) SSS differences (in kg m^{-3}). The contour intervals are 0.08 (see the main text

570 for details of the decomposition method). (f): Sea surface density differences
571 estimated from SST differences, assuming a uniform thermal expansion
572 coefficient (i.e. (a) multiplied by $-0.22 \text{ kg } ^\circ\text{C}^{-1} \text{ m}^{-3}$) (in kg m^{-3}). The contour intervals
573 are 0.08. (g), as in (f), but from SSS differences assuming uniform saline
574 contraction coefficients (i.e., (b) multiplied by $0.77 \text{ kg psu}^{-1} \text{ m}^{-3}$). The sum of (f)
575 and (g) is shown in (h). (i)-(k): As in (c)-(e), but for the mixed layer depth
576 differences (in m). The contour intervals are 20. Differences that are significant
577 at the 80% confidence levels on the basis of a two-tailed t-test are green dotted
578 (except for (f)-(h)). All panels are from the Argo data.

579

Composite differences of SST, SSS, SSD, and MLD from FORA-WNP30 (Positive years - negative years)



580

581 Figure 10. As in Fig. 9, but from the FORA-WNP30.

582

583

A noticeable feature in the composite field is the fact the spatial pattern of SST's

584

contribution to SSD (Figs. 9c) is somewhat different from that of the original SST differences

585

(Figs. 9a), and such discrepancies are not found in the SSS fields (Figs. 9b, d) (see also Fig. 10

586

for the FORA-WNP30). Specifically, SST's contribution to SSD is relatively weak in higher

587 latitudes compared to the distribution of the original SST differences. This could be due to lower
588 background SST and weaker dependence of density on temperature at higher latitudes. To
589 confirm this argument, we converted SST and SSS anomalies into SSD using a linear relation.
590 Assuming the linearity of the equation of state, the differences of potential density can be
591 approximated as follows:

$$\Delta\rho = \Delta\rho_T + \Delta\rho_S \simeq \alpha(T_{POS} - T_{NEG}) + \beta(S_{POS} - S_{NEG}) = -\alpha\Delta T + \beta\Delta S,$$

592 where α and β represent thermal expansion and saline contraction coefficients, respectively. The
593 value of α significantly increases with temperature and β is almost uniform within the parameter
594 range of the upper ocean in the KOCR (Gill, 1982; Jing et al., 2019). By converting SST and
595 SSS differences into SSD using spatially constant α and β , we can estimate the impact of the
596 background SST distribution (here we choose $\alpha = 0.22 \text{ kg } ^\circ\text{C}^{-1} \text{ m}^{-3}$ and $\beta = 0.77 \text{ kg psu}^{-1} \text{ m}^{-3}$).
597 Figs. 9f-h show the SSD anomalies estimated through a linear relationship between temperature,
598 salinity, and potential density. The negative values of the SSD differences under the linear
599 relation (Fig. 9h) extend more poleward than those of the actual SSD differences (Fig. 9e),
600 primarily due to larger contributions from SST (Figs. 9c, f). Similar patterns but weaker
601 magnitudes are also evident in composites from the FORA-WNP30, again confirming the
602 importance of nonlinearity in generating SSD anomalies. We note that a recent study
603 demonstrated that differences in the thermohaline properties of mesoscale eddies in the KE and
604 those in the Oyashio region can also be explained by the meridional contrasts in the thermal
605 expansion coefficients associated with the front of background SST (Jing et al., 2019).

606 Changes in SSD can alter the density stratification, hence affecting the MLD, which is an
607 important parameter for controlling the effective heat capacity of the upper ocean. To assess the
608 impacts of temperature and salinity variations on the MLD, we also decompose the MLD

609 differences between the positive and negative years using the method described above. Here, the
610 MLD is defined as a depth at which the density increases by 0.125 kg m^{-3} over the SSD.

611 The total differences in MLD in the KOCR are characterized by a complex spatial pattern
612 with meridionally alternating positive and negative anomalies (Fig. 9k). During the positive year,
613 a significant ML shoaling is observed around $38\text{--}40^\circ\text{N}$ and $32\text{--}35^\circ\text{N}$, whereas deepening of ML
614 is observed to north of 40°N . Distinct MLD variations associated with changes in the dynamical
615 state of the KE are also pointed out by Oka et al. (2012); they have found that deepening of
616 wintertime ML is observed around $31\text{--}35^\circ\text{N}$ and $40\text{--}42^\circ\text{N}$ during a stable state of KE (see their
617 Fig. 4). Given that a positive (negative) year generally corresponds to an unstable (a stable) state
618 of KE, our results are fairly consistent with findings of Oka et al, (2012), although some
619 discrepancies are found in the details of their spatial patterns, arguably due to differences in data
620 period and processing methods.

621 A decomposition of these differences demonstrates that the ML shoaling in the KOCR
622 during positive years is limited to the south of 40°N because of the salinity effects (Fig. 9j). This
623 can be explained by an anomalous increase in SSD near the surface associated with positive SSS
624 anomalies there (Figs. 9b, d). Meanwhile, contributions from temperature anomalies dominate
625 those of salinity anomalies to the south (Fig. 9i). Again, the qualitatively same features were
626 found in composites from the FORA-WNP30 (Figs. 10i–k), but the ML shoaling in the southern
627 KOCR was also caused by salinity anomalies (around $36^\circ\text{--}38^\circ\text{N}$). Such MLD changes cannot be
628 simply explained by corresponding SSD anomalies, implying that subsurface salinity anomalies
629 also play an important role in determining the distribution of MLD.

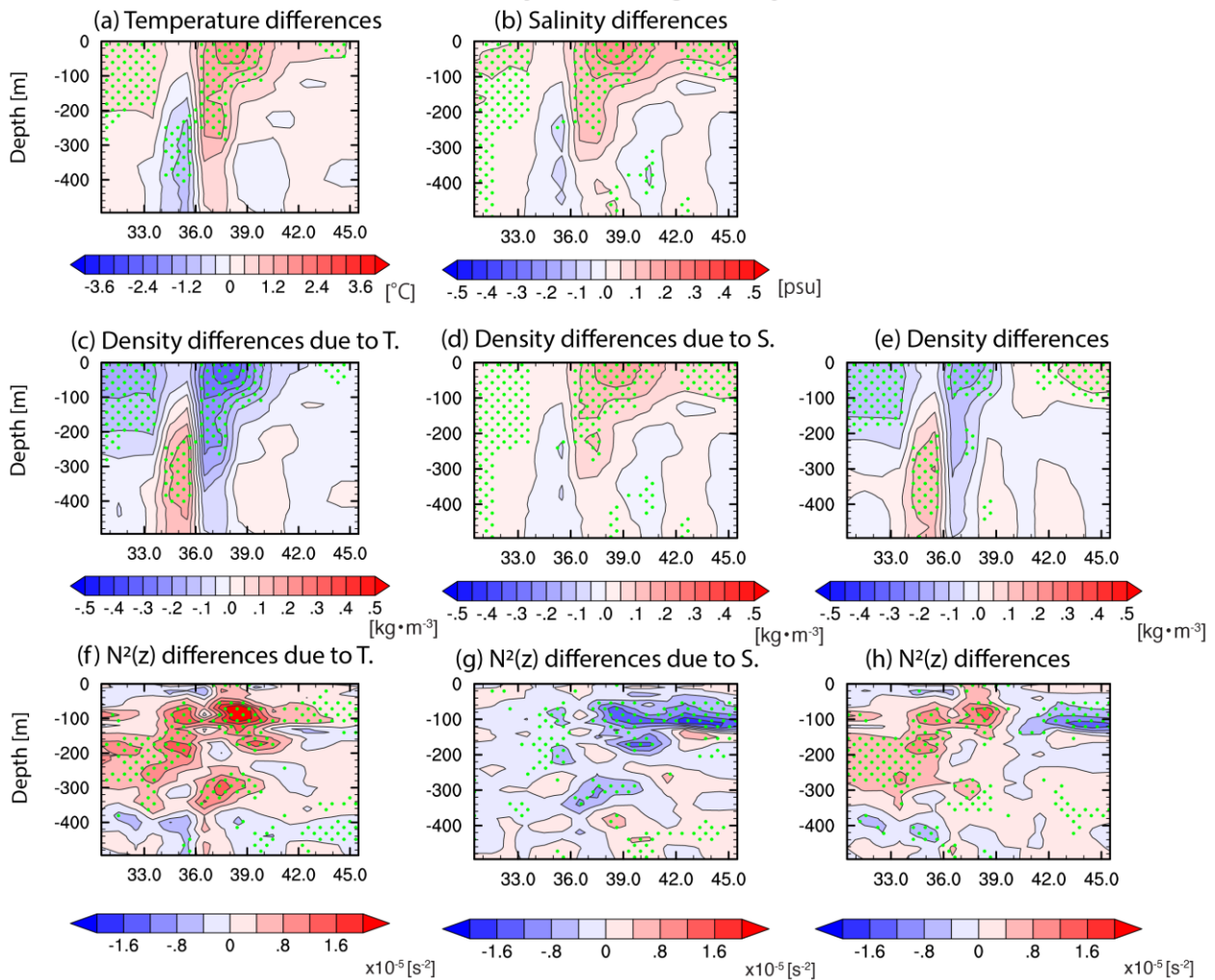
630 To highlight the vertical structure of the temperature and salinity contributions to density
631 anomalies, we constructed depth-latitude sections of the decomposed anomalies (Figs. 11 and

632 12). The anomalous high temperature and salinity near the climatological thermohaline fronts
633 (Figs. 11a, b) have their peak near the surface (thermocline depth) in the northern (southern) part
634 of the KOCR. These positive temperature and salinity anomalies generate offsetting density
635 perturbations (Figs. 11c, d).

636 Due to the larger thermal expansion coefficients for warmer water, the contributions from
637 temperature dominate the total density field to the south of 38°N, but they become comparable
638 (~80% of temperature's contribution; figure not shown) to those of salinity to the north (Fig.
639 11e). The effects of these anomalies on the density stratification can be inferred from the
640 composite of squared buoyancy frequency $N^2(z) = \frac{-g}{\rho_0} \frac{\partial \rho}{\partial z}$ (Figs. 11f–h). Here, we have
641 computed $N^2(z)$ from the density field using the central difference scheme with a uniform
642 vertical grid. For the poleward side of the KOCR (north of 38°N), positive differences in $N^2(z)$
643 (i.e., strengthening of the stratification) due to anomalous surface warming (Fig. 11f) were
644 significantly compensated by concomitant increase in salinity and potential density near the
645 surface (Fig. 11g). For the southern side, by contrast, salinity effects are not so large and total
646 differences largely reflect contributions from temperature (Figs. 11f, h). A similar meridional
647 contrast of hydrographic structures can also be seen in the composites from the FORA-WNP30
648 (Fig. 12), although subsurface differences around the KE latitude (~36°–38°N) are more
649 prominent compared to the Argo data. Both in the Argo and FORA-WNP30 products, salinity
650 variations in the KOCR have nonnegligible contributions to the density perturbations compared
651 to temperature variations, and they become comparable to those of temperature to the north of
652 38°N as the background temperature decreases poleward. Therefore, these salinity variations
653 have the potential to significantly affect the strength of the vertical mixing and evolution of

654 temperature, which will be carefully quantified in the next section using the 1-D ML model
 655 experiments.
 656

**Composite differences of temperature, salinity, density, and $N^2(z)$ from Argo
 (Positive years- negative years)**

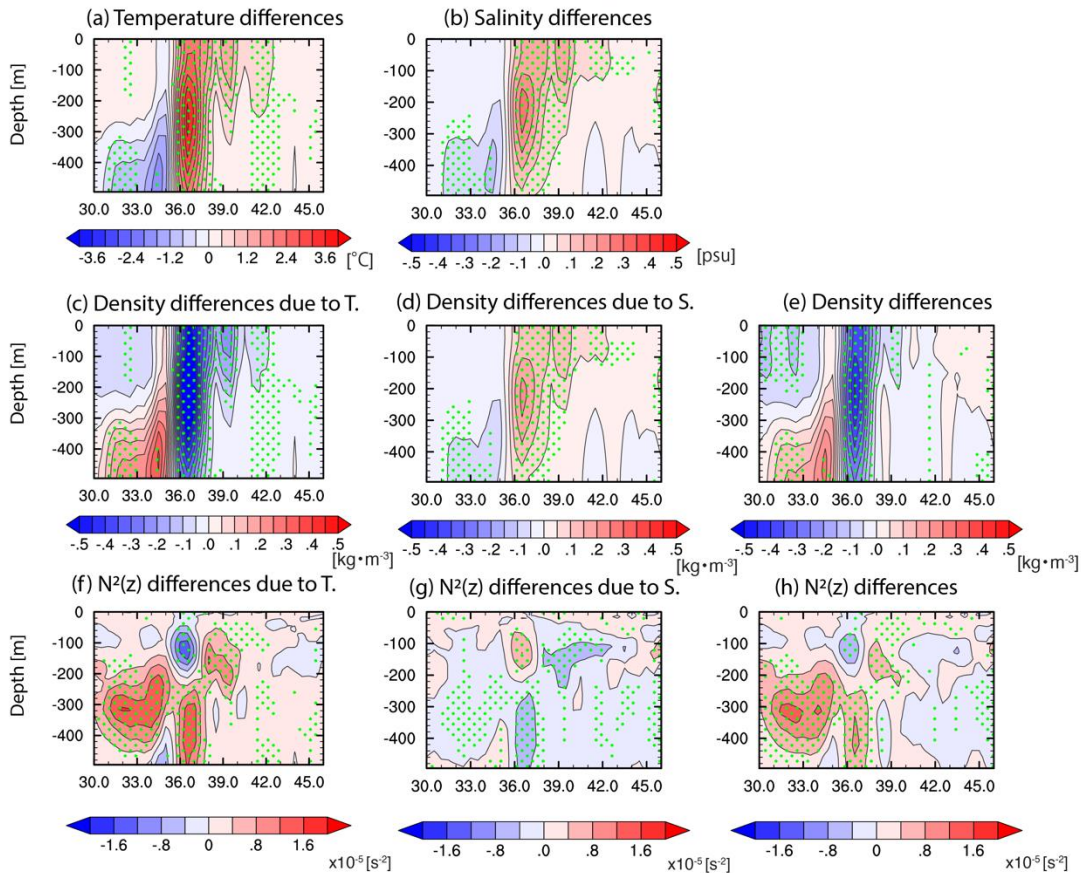


657
 658 Figure 11. (a): Latitude-depth section of composited temperature differences
 659 between positive and negative years during February-April from the Argo data
 660 (in °C). The contour intervals are 0.4. (b): As in (a), but for salinity differences (in
 661 psu). The contour intervals are 0.05. (c)-(e): As in (a) and (b), but for (e) density

662 differences and contribution from (c) temperature and (d) salinity differences (in
 663 kg m^{-3}). The contour intervals are 0.05. (f)-(h): As in (c)-(e), but for the squared
 664 buoyancy frequency anomalies (in s^{-2}). The contour intervals are 4×10^{-6} . The
 665 differences that are significant at the 80% confidence levels on the basis of a
 666 two-tailed t-test are green dotted.

667

**Composite differences of temperature, salinity, density, and $N^2(z)$ from FORA-WNP30
 (Positive years- negative years)**



668

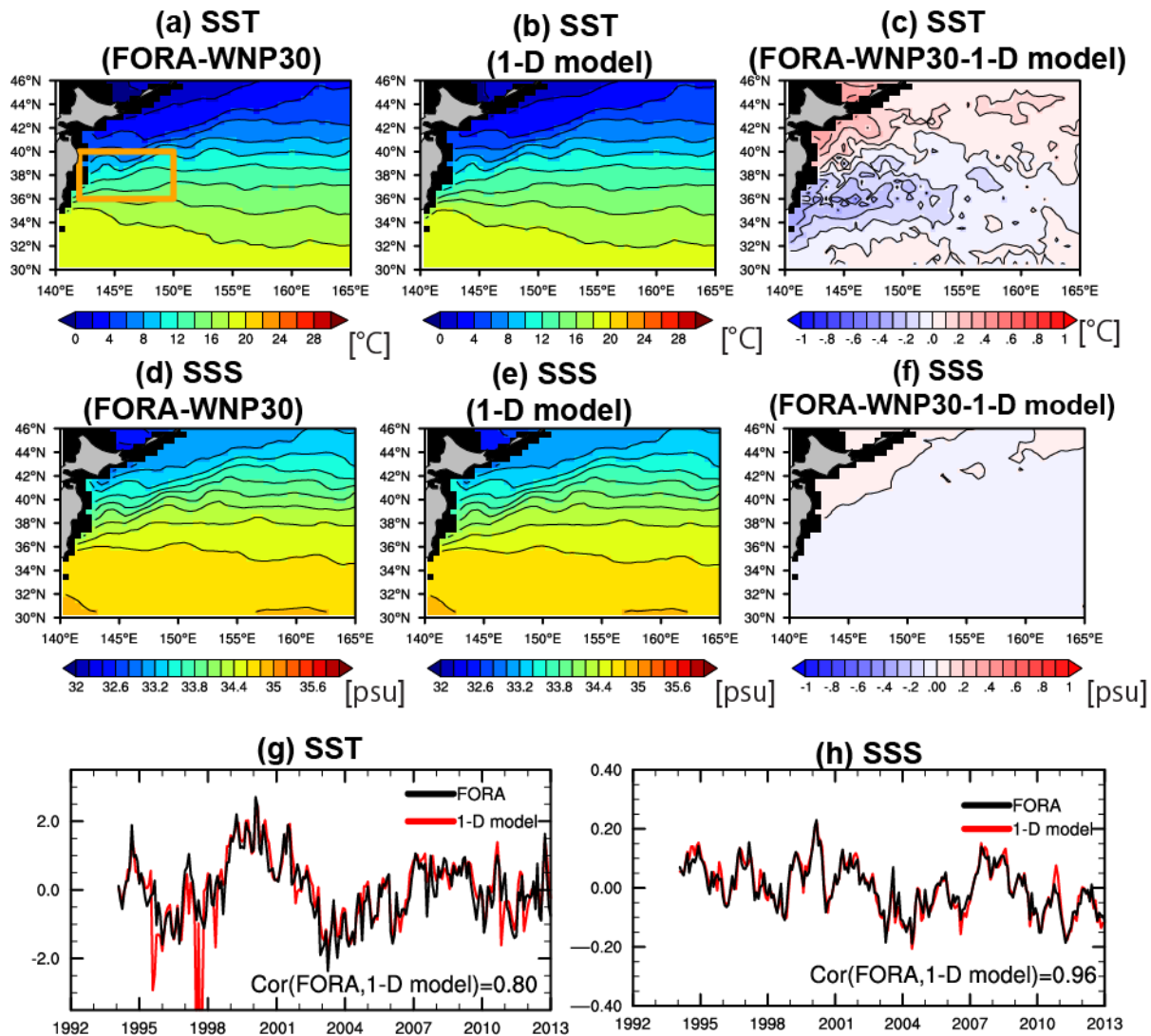
669 Figure 12. As in Fig. 11, but from the FORA-WNP30.

670 **4.2 Quantitative assessment using 1-D model**

671 Before proceeding to sensitivity experiments of the 1-D ML model, we first check the
672 performance of our control (CTL) experiment, which is a reference for the sensitivity
673 experiments. In the CTL experiment, the model is driven by atmospheric forcing from the J-
674 OFURO3, geostrophic current fields from the FORA-WNP30, and temperature and momentum
675 dynamical correction terms derived from the preliminary experiment, whereas the modeled
676 salinity is strongly nudged toward the values of the FORA-WNP30, as detailed in Section 2.2.
677 Owing to the implementation of the dynamical correction methods, the model aptly captures the
678 spatial pattern of the climatological SST and SSS fields (Figs. 13a–f), although the modeled SST
679 is slightly warmer (cooler) to the north (south) of 40°N compared to that of the FORA-WNP30.
680 Here, we have shown the wintertime mean state as a representative period with strong SST/SSS
681 fronts; however, the climatology of other seasons, such as the March–May averaged field, is also
682 simulated well by the 1-D model. In addition, the climatology of the subsurface temperature and
683 salinity fields, as well as the horizontal currents, is also in good agreement with the reanalysis
684 product (figures not shown). This suggests that our 1-D model can adequately simulate the
685 background oceanic conditions over the western North Pacific. Furthermore, the time evolutions
686 of area-averaged SST anomalies over the KOCR from the FORA-WNP30 and the 1-D model are
687 also compared well (Fig. 13g). Similarly, the SSS variation in the 1-D model also corresponds
688 well with that in the reanalysis product (Fig. 13h), as was expected from the adoption of salinity
689 nudging during the CTL experiment. These conspicuous agreements between the 1-D ML model
690 and the reanalysis product allow us to make further use of it for a more detailed investigation.

691

692



693
 694 Figure 13. (a), (b): Climatological SST during January-March from (a) the FORA-
 695 WNP30 and (b) the CTL experiment of the 1-D ML model (in °C). The differences
 696 between (a) and (b) are shown in (c). The contour intervals in (a) and (b) are 2,
 697 whereas those in (c) are 0.1. (d)-(f): As in (a)-(c), but for SSS (in psu). The contour
 698 intervals in (d) and (e) are 0.2, whereas those in (f) are 0.1. (g): Time series of
 699 area-averaged SST anomalies over the KOCR (see the orange box in (a)) from the

700 FORA-WNP30 (black) and 1-D ML model (red). The correlation coefficient between
701 them is shown in the lower right. (h) As in (g), but for SSS anomalies.

702

703 While both temperature and salinity variability are dominated by the same 3-D
704 mechanisms as discussed above, here we intend to clarify how and to what extent salinity has
705 potential to modify dynamical and thermodynamical processes in the upper ocean. Motivated by
706 the fact that many previous studies on the KOCR have not explicitly considered the salinity
707 effects mainly due to limited salinity observations, we explore this issue with an artificial
708 experiment with the 1-D model. To explicitly depict the role played by salinity variability, we
709 treat salinity as a “forcing” in the 1-D ML model and see “responses” of other related variables,
710 such as the vertical diffusion coefficients and temperature. Based on this concept, we have
711 designed another set of experiments that nullify the salinity’s roles by artificially suppressing its
712 fluctuation (referred to as the climatological salinity (Sclim) experiment). In this experiment, we
713 initialize and force the model as in the CTL experiment, except that salinity used for the initial
714 and restoring conditions was replaced by corresponding climatological values. With sufficiently
715 strong relaxation, salinity variations (except for the seasonal cycle) and associated changes in
716 density stratification and related processes are eliminated. As the same temperature and
717 momentum dynamical correction were used in both the CTL and Sclim experiments, the
718 collective impacts of salinity anomalies on the vertical mixing process and associated changes in
719 temperature can be adequately measured by considering difference between the CTL and Sclim
720 experiments (Kido & Tozuka, 2017). This framework provides useful insights regarding the
721 significance of salinity effects, although it has an inevitable limitation due to its absence of three-
722 dimensional responses (e.g., possible changes in temperature advection associated with salinity-

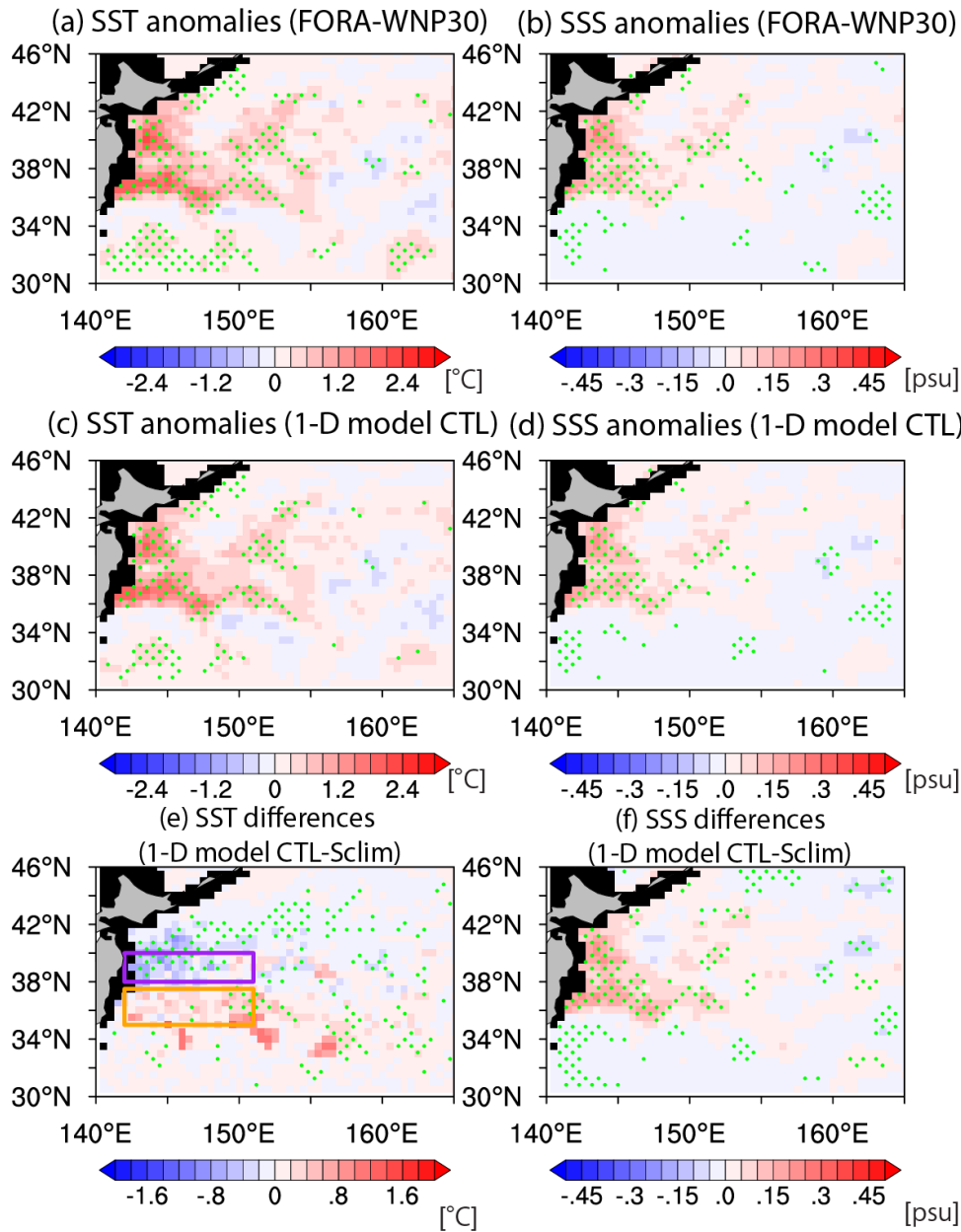
723 induced current anomalies are not included). Because oceanic anomalies during negative years
724 are close to a mirror image of those during positive years, we only conducted the Sclim
725 experiment for the seven positive years appeared in the FORA-WNP30 (see Table 1).

726 The observed anomalous surface warming and saltening over the KOCR during the late
727 winter to spring of the positive years (Figs. 14a, b) were well reproduced in the CTL experiment
728 (Figs. 14c, d), further confirming its satisfactory ability to simulate the observed variability. To
729 isolate the effects of salinity anomalies, we calculated the differences in the SST and SSS fields
730 between the CTL and Sclim experiments for all selected positive years and their composites, as
731 shown in Figs. 14e, f. The spatial pattern of the SSS differences between the two experiments
732 (Fig. 14f) closely resembles the composite SSS anomalies (Fig. 14d; see also Figs. 3f and 4f),
733 suggesting that the targeted SSS anomalies over the KOCR were successfully removed in the
734 Sclim experiment. The SST differences were characterized by negative (positive) values over the
735 northern (southern) part of the KOCR, suggesting that the inclusion of salinity anomalies during
736 positive years led to cooling (warming) in those parts (Fig. 14e). This implies that salinity
737 variations during the positive years serve to dampen (amplify) the concomitant SST warming
738 over the northern (southern) part of the KOCR and hence, inhibit the poleward intrusion of
739 anomalous warming. The areas with cooler (warmer) SST in the CTL than the Sclim experiment
740 roughly coincide with the regions where salinity anomalies contribute to the weakening
741 (strengthening) of density stratification and deepening (shoaling) of the mixed layer, indicating
742 that changes in the vertical process may hold the key. These differences are commonly seen in
743 all positive years and the maximum differences in SST between the two experiments reaches
744 1.0°C, which constitutes 20%–40% of the total SST anomalies there (Figs. 14c, e). Therefore,

745 salinity variations in the KOCR can exert significant effects on the evolution of SST therein by
 746 modulating the 1-D vertical process.

747

Composite of SST and SSS anomalies from FORA-WNP30 and 1-D model (Positive years)



748

749 Figure 14. (a), (b): Composite of (a) SST (in °C) and (b) SSS (in psu) anomalies
750 during February-April during positive years from the FORA-WNP30. (c), (d): As in
751 (a) and (b), but from the CTL experiment of the 1-D ML model. (e), (f): Composite
752 of the difference in SST (e) and SSS (f) between the CTL and Sclim experiments
753 of the 1-D ML model during March-May. The green dotted regions indicate
754 differences that are significant at the 80% confidence levels on the basis of a
755 two-tailed t test. The purple and orange boxes in (e) denote the northern and
756 southern box, respectively.

757

758 What causes such distinct SST differences between the two experiments? Given the
759 configurations of our 1-D ML model experiments, there are two possible explanations for these
760 differences. First, changes in the MLD due to salinity anomalies (cf. Figs. 9i–k and 10i–k) can
761 alter the effective heat capacity of the upper ocean and affect the sensitivity of SST to
762 atmospheric heat flux. Second, changes in vertical stratification due to salinity anomalies may
763 modulate the strength of vertical mixing and turbulent heat transport in the upper ocean. To
764 assess the first hypothesis, we carried out a detailed mixed layer heat budget analysis based on
765 the output from the 1-D ML model (see the supplementary material for details), and it was found
766 that the MLD changes due to salinity anomalies have the opposite effect. These results indicate
767 that the SST differences between the two experiments cannot be simply explained by those in the
768 atmospheric heat flux or MLD, implying that modulations in vertical mixing and associated heat
769 transport hold the key.

770 To confirm the above statement and further illuminate the related physical processes, we
771 next check the time evolution of other mixing-related parameters, such as the density
772 stratification and vertical mixing coefficient from each experiment. The time-depth plots of the
773 area-averaged composited temperature, salinity, squared buoyancy frequency ($N^2(z)$), and
774 vertical diffusion coefficient of temperature (κ_T : see Eq. 1) from both 1-D ML model
775 experiments are shown in Figs. 15 (the northern box) and 16 (the southern box).

776 For the northern box, the seasonal cycle of temperature and salinity variation, such as the
777 gradual deepening of the mixed layer in winter and rapid shoaling during spring, are reproduced
778 in both experiments, (Figs. 15a, b, d, e). Differences between the CTL and Sclim experiments
779 demonstrate that the positive salinity anomalies near the surface begin to develop in winter, peak
780 in spring, and subsequently decay in summer (Fig. 15f). These salinity anomalies serve to
781 weaken upper ocean stratification at 100–150 m depth (Fig. 15i) and then lead to the
782 strengthening of the vertical mixing there (Fig. 15l). As a result, the vertical heat exchange
783 between the surface and subsurface layer during late winter to early spring is greatly enhanced,
784 giving rise to cooler SST and a warmer subsurface temperature in the CTL experiment (Fig. 15c),
785 supporting the hypothesis proposed above. We again note that temperature differences between
786 the CTL and Sclim experiments are caused only by changes in the vertical diffusion because
787 both experiments adopt the same amount of dynamical corrections and shortwave radiation. Thus,
788 the chain of physical processes described above is adequately represented in our experimental
789 framework. The maximum SST differences were found during April–May and then subducted
790 below the seasonal thermocline during summer and fall. Differences in the subsurface
791 temperature (i.e., warmer temperatures in the CTL experiment) at 150–200 m depth also persist
792 through summer and remain until fall, even though no salinity signals survive until this season.

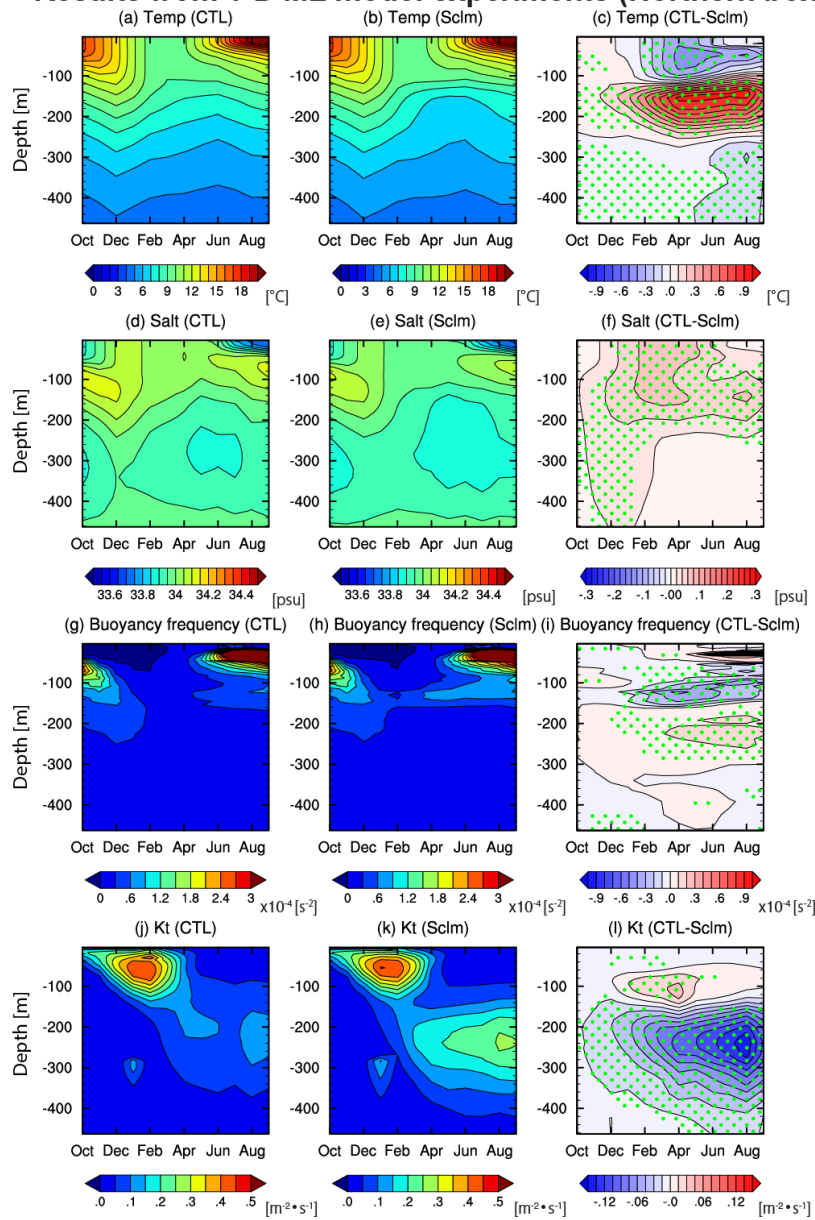
793 Therefore, the salinity-induced temperature perturbations can persist longer than the salinity
794 variations themselves and hence have the potential to affect the low-frequency variation of upper
795 ocean.

796 The 1-D ML model also satisfactorily reproduces the key features of temperature and
797 salinity variation within the southern box (Figs. 16a–f), as in the northern box. Significant
798 positive salinity signals are also evident in the difference between the two experiments, but their
799 maximum peak is found at 100–150 m depth rather than near the surface (Figs. 16d–f).
800 Consequently, the density stratification is strengthened (Fig. 16i) and vertical mixing near the
801 thermocline is substantially more suppressed in the CTL experiment than in the Sclim
802 experiment (Fig. 16l). Therefore, the vertical entrainment of subsurface cold water is
803 significantly reduced, and eventually leads to a warmer SST (and slightly lower thermocline
804 temperature) in the CTL experiment.

805

806

Results from 1-D ML model experiments (Northern box)

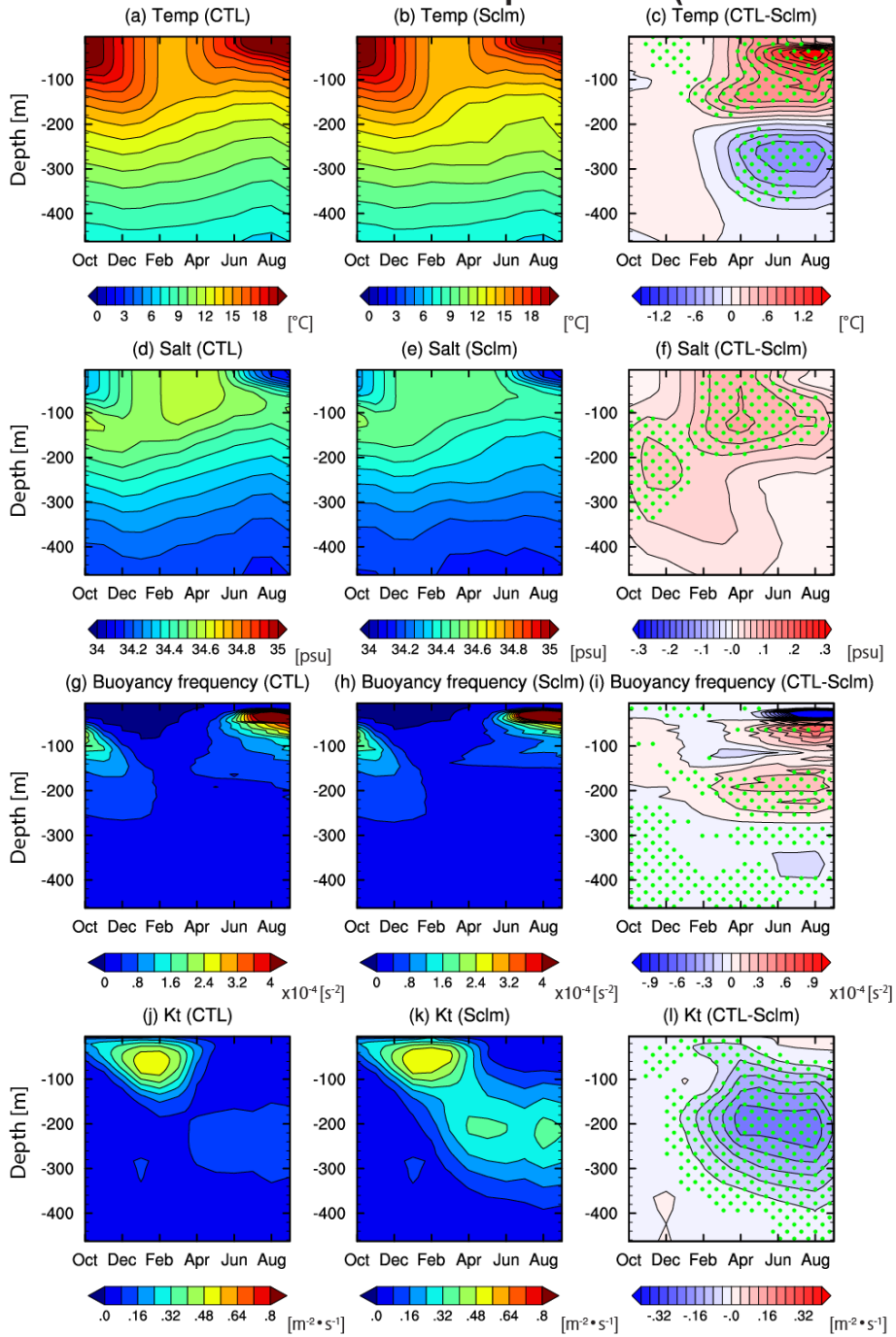


807

808 Figure 15. (a)-(c): Time evolution of composited temperature in (a) CTL and (b)
 809 Sclm experiments during positive years (in °C), and (c) their difference (i.e., CTL
 810 minus the Sclm experiments) averaged over the northern box (142°E-151°E, 38°N-
 811 40°N: See the purple box in Fig. 14e). The contour intervals in (a) and (b) are 1,
 812 whereas those in (c) are 0.1. The differences that are significant at the 80%

813 confidence levels on the basis of a two-tailed t-test are green dotted in (c). (d)-
814 (f): As in (a)-(c), but for salinity (in psu). The contour intervals in (d) and (e) are
815 0.05, whereas those in (f) are 0.03. (g)-(i): As in (a)-(c), but for the squared
816 buoyancy frequency (in s^{-2}). The contour intervals are 3×10^{-5} . (j)-(l): As in (a)-(c),
817 but for the vertical diffusion coefficients (in $m^2 s^{-1}$). The contour intervals are
818 5×10^{-2} .
819

Results from 1-D ML model experiments (Southern box)



820

821 Figure 16. As in Fig. 15, but for the southern box (142°E-151°E, 35°N-37°N: See

822 the purple box in Fig. 14e).

823 **5. Summary and discussion**

824 Using observational datasets and an eddy-resolving ocean reanalysis product (FORA-
825 WNP30), in this study, we investigated low-frequency variations of upper ocean salinity in the
826 KOCR and examined their mechanism and possible effects on the mixed-layer processes, with a
827 specific focus on variability during the boreal winter to spring. From a gridded dataset based on
828 the Argo profiles and an eddy-resolving ocean reanalysis product, we identified a coherent
829 interannual to decadal variation in temperature and salinity in the KOCR, with anomalous
830 saltening (freshening) tending to be accompanied by significant warming (cooling) across the
831 same region. Based on the area-averaged SST and SSS anomalies in the KOCR, we selected
832 several typical years for such events, and a positive (negative) year is defined as one with a
833 significant increase (decrease) in both SST and SSS in the area. A close inspection of the three-
834 dimensional structures of composite temperature and salinity anomalies reveals that such
835 anomalies are concentrated near the surface in the northern part of the KOCR, but strong
836 anomalies are found at 200–400 m depth in the southern part of the KOCR. Such meridional
837 differences in the vertical structures of thermohaline anomalies reflect the distribution of the
838 climatological temperature and salinity fronts, which was also pointed out by earlier works
839 (Nakamura & Kazmin, 2003; Nonaka et al., 2006).

840 The mechanisms of these salinity variations were then explored based on the basis of a
841 composite and lag correlation analysis of the related physical variables. We found that the
842 dynamical stability of the KE was the predominant factor behind the observed variations. During
843 positive years, accompanying an unstable state of the KE, an increase in the SSH and anomalous
844 anticyclonic circulation could be observed in the northern part of the KE. Further, associated
845 northeastward current anomalies directing toward the KOCR enhanced the poleward transport of

846 warm and saline water originating from the subtropics, leading to significant surface warming
847 and saltening in the KOCR. At the same time, the intensification of mesoscale eddy activity and
848 eddy-induced advection in the upstream of the KE also contribute to the generation of positive
849 temperature and salinity anomalies in the KOCR. The increase in surface evaporation due to
850 positive SST anomalies also serves to maintain the positive SSS in the KOCR, but its
851 contribution is relatively small compared to the ocean dynamical effects mentioned above.
852 Similar anomalies, but with opposite polarities (i.e., features with a stable state of the KE) also
853 contribute to anomalous cooling and freshening during negative years.

854 To quantify the effects of these salinity variations on the density of seawater and vertical
855 stratification, we decomposed the density anomalies into contributions from temperature and
856 salinity anomalies. During the positive years, positive SSS anomalies in the northern part of the
857 KOCR lead to an increase in surface density and serve to deepen the mixed layer in that region.
858 Similarly, the positive subsurface salinity anomalies in the southern part of the KOCR enhance
859 the vertical stability and contribute to the shoaling of the mixed layer by increasing the density at
860 that depth. These salinity-induced density perturbations compensate for the concomitant
861 temperature-induced density perturbations and significantly reduce the amplitude of total
862 anomalies. Salinity contributions to density anomalies increase poleward and become
863 comparable to those of temperature in the northern part of the KOCR, and this can be explained
864 by the weaker dependence of density on temperature due to lower background temperatures in
865 that region. These results suggest that salinity variations in the KOCR have substantial impacts
866 on the local density fields and may exert considerable effects on dynamical and
867 thermodynamical processes.

868 Based on the results from the density decomposition, we have assessed the impacts of the
869 density changes associated with salinity anomalies upon the strength of vertical mixing and
870 evolution of the upper ocean temperature by carefully designing and conducting a series of
871 sensitivity experiments using the 1-D ML model. These sensitivity experiments demonstrated
872 that salinity anomalies during positive years serve to cool SST in the northern part of the KOCR
873 by up to -1.0°C , whereas in the southern part, they cause SST warming of the same amplitude.
874 By analyzing other variables from the 1-D ML model, it was found that changes in density
875 stratification due to salinity anomalies indeed modulate the strength of vertical mixing and
876 induce significant responses in the upper ocean temperature. More specifically, positive SSS
877 anomalies in the northern part of the KOCR reduce the density stratification and strengthen the
878 vertical mixing in that region, resulting in significant near surface cooling and subsurface
879 warming in that region. In the southern part, by contrast, positive subsurface salinity anomalies
880 during positive years stabilize the upper ocean column and suppress the vertical exchange of heat
881 within the mixed layer, leading to near surface warming and (weaker) subsurface cooling. Thus,
882 surface and subsurface salinity anomalies in the KOCR suppress the poleward expansions of co-
883 occurring temperature anomalies.

884 The close linkage between the dynamical states of the KE and SST variations over the
885 KOCR has been documented in several previous studies (Masunaga et al., 2016; Qiu et al., 2017;
886 Sasaki & Minobe, 2015; Sugimoto et al., 2014). However, little has been discovered concerning
887 the concomitant salinity variations and associated mechanisms. In this regard, we have shown,
888 primarily based on a lagged correlation analysis, that ocean dynamical processes, especially the
889 modulation of heat and salt transport by large-scale circulation and mesoscale eddies, are closely
890 related to the wintertime temperature and salinity variations in the KOCR. Although these

891 conclusions are physically consistent and in accordance with many previous studies, they are still
892 based on statistical relationships and more physical approaches are required to confirm their
893 validity. An accurate salinity budget analysis as well as coordinated sensitivity experiments
894 using high-resolution ocean general circulation models (OGCMs) would be helpful in addressing
895 these issues.

896 In this study, we demonstrated that salinity has the potential to play an active role in low-
897 frequency variations in the KOCR by modulating the upper ocean temperature via density
898 change. These results have important implications for the study of climate variability in the
899 North Pacific, as the SST variability in the KOCR affects atmospheric circulation, as discussed
900 in Section 1 (Frankignoul et al., 2011; Taguchi et al., 2012). Due to the strong internal variability
901 of the atmosphere and ocean, how and to what extent these atmospheric responses to SST
902 anomalies feed back onto the ocean is still a matter for debate, but salinity may be involved in
903 such feedback processes, provided that it exerts strong impacts on SST. An important caveat of
904 this study is that our estimates of salinity impacts on SST based on the 1-D ML model disregard
905 changes in three-dimensional advective processes produced by salinity anomalies. As salinity
906 anomalies may also alter circulation in the upper ocean and the associated transport of heat and
907 momentum, well-designed OGCM and data assimilation experiments are necessary to
908 incorporate and assess the significance of such effects. Finally, strong salinity fronts are also
909 found in other WBCs such as the Gulf Stream, Agulhas Current, and Antarctic Circumpolar
910 Current (Kida et al., 2015; Ohishi et al., 2019), and similar salinity variations may also be
911 evident in these regions. The applications of our approach to other WBCs and comparisons to the
912 KOCR results will provide further insight into the physical processes operating in the WBCs and
913 their roles in midlatitude climate variability.

914 **Acknowledgments**

915 We would like to thank Tomoki Tozuka, Eitarou Oka, and Shota Katsura for their
916 insightful comments and suggestions, and Norihisa Usui for his technical advice on the use of
917 FORA- Constructive comments from two anonymous reviewers have significantly improved an
918 early version of the manuscript. Data used were obtained as follows; the gridded Argo product
919 from the Scripps Institution of Oceanography is from [http://sio-
920 argo.ucsd.edu/RG_Climatology.html](http://sio-argo.ucsd.edu/RG_Climatology.html); the FORA-WNP30 data is from
921 <http://synthesis.jamstec.go.jp/FORA/e/index.html>; and the J-OFURO3 surface flux data is from
922 <https://j-ofuro.isee.nagoya-u.ac.jp/en/>. The present study is supported by KAKENHI
923 JP19H05701, JP19H05702, JP18H03726, and 21K13997.

924
925

926 **References**

- 927
- 928 Dong, D., Brandt, P., Chang, P., Schütte, F., Yang, X., Yan, J., & Zeng, J. (2017). Mesoscale
929 eddies in the northwestern Pacific Ocean: Three-dimensional eddy structures and heat/salt
930 transports. *Journal of Geophysical Research: Oceans*, *122*(12), 9795–9813.
931 <https://doi.org/10.1002/2017JC013303>
- 932 Duchon, C. E. (1979). Lanczos filtering in one and two dimensions. *Journal of Applied*
933 *Meteorology*, *18*(8), 1016–1022. [https://doi.org/10.1175/1520-](https://doi.org/10.1175/1520-0450(1979)018<1016:LFIOAT>2.0.CO;2)
934 [0450\(1979\)018<1016:LFIOAT>2.0.CO;2](https://doi.org/10.1175/1520-0450(1979)018<1016:LFIOAT>2.0.CO;2)
- 935 Frankignoul, C., Sennéchaël, N., Kwon, Y.-O., & Alexander, M. A. (2011). Influence of the
936 meridional shifts of the Kuroshio and the Oyashio Extensions on the atmospheric
937 circulation. *Journal of Climate*, *24*(3), 762–777. <https://doi.org/10.1175/2010JCLI3731.1>
- 938 Furuichi, N., Hibiya, T., & Niwa, Y. (2012). Assessment of turbulence closure models for
939 resonant inertial response in the oceanic mixed layer using a large eddy simulation model.
940 *Journal of Oceanography*, *68*(2), 285–294. <https://doi.org/10.1007/s10872-011-0095-3>
- 941 Geng, Y., Wang, Q., & Mu, M. (2018). Effect of the Decadal Kuroshio Extension Variability on
942 the Seasonal Changes of the Mixed-Layer Salinity Anomalies in the Kuroshio-Oyashio
943 Confluence Region. *Journal of Geophysical Research: Oceans*, *123*(12), 8849–8861.
944 <https://doi.org/10.1029/2018JC014139>
- 945 Gill, A. E. (1982). *Atmosphere Ocean dynamics* (Internatio). Academic Press.
- 946 Hasson, A. E. A., Delcroix, T., & Dussin, R. (2013). An assessment of the mixed layer salinity
947 budget in the tropical Pacific Ocean. Observations and modelling (1990-2009). *Ocean*
948 *Dynamics*, *63*(2–3), 179–194. <https://doi.org/10.1007/s10236-013-0596-2>
- 949 Hosoda, S., Ohira, T., & Nakamura, T. (2008). A monthly mean dataset of global oceanic
950 temperature and salinity derived from Argo float observations. *JAMSTEC Report of*
951 *Research and Development*, *8*(November), 47–59. <https://doi.org/10.5918/jamstecr.8.47>
- 952 Isoguchi, O., Kawamura, H., & Oka, E. (2006). Quasi-stationary jets transporting surface warm
953 waters across the transition zone between the subtropical and the subarctic gyres in the
954 North Pacific. *Journal of Geophysical Research*, *111*(C10), C10003.
955 <https://doi.org/10.1029/2005JC003402>
- 956 Itoh, S., & Yasuda, I. (2010). Characteristics of mesoscale eddies in the Kuroshio–Oyashio
957 extension region detected from the distribution of the sea surface height anomaly. *Journal*

958 of *Physical Oceanography*, 40(5), 1018–1034. <https://doi.org/10.1175/2009JPO4265.1>

959 Jackett, D. R., & Mcdougall, T. J. (1995). Minimal Adjustment of Hydrographic Profiles to

960 Achieve Static Stability. *Journal of Atmospheric and Oceanic Technology*.

961 [https://doi.org/10.1175/1520-0426\(1995\)012<0381:maohpt>2.0.co;2](https://doi.org/10.1175/1520-0426(1995)012<0381:maohpt>2.0.co;2)

962 Jing, Z., Chang, P., Shan, X., Wang, S., Wu, L., & Kurian, J. (2019). Mesoscale SST dynamics

963 in the Kuroshio-Oyashio extension region. *Journal of Physical Oceanography*, 49(5), 1339–

964 1352. <https://doi.org/10.1175/JPO-D-18-0159.1>

965 Kara, A. B., Hurlburt, H. E., & Wallcraft, A. J. (2005). Stability-dependent exchange coefficients

966 for air-sea fluxes. *Journal of Atmospheric and Oceanic Technology*, 22(7), 1080–1094.

967 <https://doi.org/10.1175/JTECH1747.1>

968 Kelly, K. A., Small, R. J., Samelson, R. M., Qiu, B., Joyce, T. M., Kwon, Y.-O., & Cronin, M. F.

969 (2010). Western boundary currents and frontal air-sea interaction: Gulf stream and Kuroshio

970 Extension. *Journal of Climate*, 23(21), 5644–5667. <https://doi.org/10.1175/2010JCLI3346.1>

971 Kida, S., Mitsudera, H., Aoki, S., Guo, X., Ito, S. ichi, Kobashi, F., et al. (2015). Oceanic fronts

972 and jets around Japan: a review. *Journal of Oceanography*, 71(5), 469–497.

973 <https://doi.org/10.1007/s10872-015-0283-7>

974 Kido, S., & Tozuka, T. (2017). Salinity variability associated with the positive Indian Ocean

975 Dipole and its impact on the upper ocean temperature. *Journal of Climate*, 30(19), 7885–

976 7907. <https://doi.org/10.1175/JCLI-D-17-0133.1>

977 Kido, S., Tozuka, T., & Han, W. (2019a). Anatomy of salinity anomalies associated with the

978 positive Indian Ocean Dipole. *Journal of Geophysical Research: Oceans*, 124(11), 8116–

979 8139. <https://doi.org/10.1029/2019JC015163>

980 Kido, S., Tozuka, T., & Han, W. (2019b). Experimental assessments on impacts of salinity

981 anomalies on the positive Indian Ocean Dipole. *Journal of Geophysical Research: Oceans*,

982 124(12), 9462–9486. <https://doi.org/10.1029/2019JC015479>

983 Kitamura, T., Nakano, T., & Sugimoto, S. (2016). Decadal variations in mixed layer salinity in

984 the Kuroshio Extension recirculation gyre region: influence of precipitation during the

985 warm season. *Journal of Oceanography*. <https://doi.org/10.1007/s10872-015-0317-1>

986 Kobayashi, S., Ota, Y., Harada, Y., Ebita, A., Moriya, M., Onoda, H., et al. (2015). The JRA-55

987 Reanalysis: General Specifications and Basic Characteristics. *Journal of the Meteorological*

988 *Society of Japan. Ser. II*, 93(1), 5–48. <https://doi.org/10.2151/jmsj.2015-001>

- 989 Kwon, Y.-O., & Deser, C. (2007). North Pacific decadal variability in the community climate
990 system model version 2. *Journal of Climate*, 20(11), 2416–2433.
991 <https://doi.org/10.1175/JCLI4103.1>
- 992 Kwon, Y.-O., Alexander, M. A., Bond, N. A., Frankignoul, C., Nakamura, H., Qiu, B., &
993 Thompson, L. A. (2010). Role of the Gulf Stream and Kuroshio-Oyashio systems in large-
994 scale atmosphere-ocean interaction: A review. *Journal of Climate*, 23(12), 3249–3281.
995 <https://doi.org/10.1175/2010JCLI3343.1>
- 996 Li, J., Liang, C., Tang, Y., Liu, X., Lian, T., Shen, Z., & Li, X. (2018). Impacts of the IOD-
997 associated temperature and salinity anomalies on the intermittent equatorial undercurrent
998 anomalies. *Climate Dynamics*, 51(4), 1391–1409. [https://doi.org/10.1007/s00382-017-3961-](https://doi.org/10.1007/s00382-017-3961-x)
999 x
- 1000 Ma, X., Chang, P., Saravanan, R., Montuoro, R., Hsieh, J. S., Wu, D., et al. (2015). Distant
1001 Influence of Kuroshio Eddies on North Pacific Weather Patterns? *Scientific Reports*, 5, 1–7.
1002 <https://doi.org/10.1038/srep17785>
- 1003 Masunaga, R., Nakamura, H., Miyasaka, T., Nishii, K., & Qiu, B. (2016). Interannual
1004 modulations of oceanic imprints on the wintertime atmospheric boundary layer under the
1005 changing dynamical regimes of the Kuroshio Extension. *Journal of Climate*, 29(9), 3273–
1006 3296. <https://doi.org/10.1175/JCLI-D-15-0545.1>
- 1007 Masuzawa, J. (1969). Subtropical mode water. *Deep Sea Research and Oceanographic Abstracts*,
1008 16(5), 463–472. [https://doi.org/10.1016/0011-7471\(69\)90034-5](https://doi.org/10.1016/0011-7471(69)90034-5)
- 1009 Nagano, A., Uehara, K., Suga, T., Kawai, Y., Ichikawa, H., & Cronin, M. F. (2014). Origin of
1010 near-surface high-salinity water observed in the Kuroshio Extension region. *Journal of*
1011 *Oceanography*, 70(4), 389–403. <https://doi.org/10.1007/s10872-014-0237-5>
- 1012 Nakamura, H., & Kazmin, A. S. (2003). Decadal changes in the North Pacific oceanic frontal
1013 zones as revealed in ship and satellite observations. *Journal of Geophysical Research*,
1014 108(C3), 3078. <https://doi.org/10.1029/1999JC000085>
- 1015 Nakamura, H., Lin, G., & Yamagata, T. (1997). Decadal Climate Variability in the North Pacific
1016 during the Recent Decades. *Bulletin of the American Meteorological Society*, 78(10), 2215–
1017 2225. [https://doi.org/10.1175/1520-0477\(1997\)078<2215:DCVITN>2.0.CO;2](https://doi.org/10.1175/1520-0477(1997)078<2215:DCVITN>2.0.CO;2)
- 1018 Nakamura, H., Sampe, T., Tanimoto, Y., & Shimpo, A. (2004). Observed associations among
1019 storm tracks, jet streams and midlatitude oceanic fronts. *Geophysical Monograph Series*,

1020 147, 329–345. <https://doi.org/10.1029/147GM18>

1021 Nan, F., Yu, F., Xue, H., Wang, R., & Si, G. (2015). Ocean salinity changes in the northwest
1022 Pacific subtropical gyre: The quasi-decadal oscillation and the freshening trend. *Journal of*
1023 *Geophysical Research: Oceans*, 120(3), 2179–2192. <https://doi.org/10.1002/2014JC010536>

1024 Nonaka, M., Nakamura, H., Tanimoto, Y., Kagimoto, T., & Sasaki, H. (2006). Decadal
1025 variability in the Kuroshio–Oyashio extension simulated in an eddy-resolving OGCM.
1026 *Journal of Climate*, 19(10), 1970–1989. <https://doi.org/10.1175/JCLI3793.1>

1027 Nonaka, M., Nakamura, H., Tanimoto, Y., & Sasaki, H. (2008). Interannual-to-decadal
1028 variability in the Oyashio and its influence on temperature in the subarctic frontal zone: An
1029 eddy-resolving OGCM simulation. *Journal of Climate*, 21(23), 6283–6303.
1030 <https://doi.org/10.1175/2008JCLI2294.1>

1031 Nonaka, M., Sasaki, H., Taguchi, B., & Nakamura, H. (2012). Potential predictability of
1032 interannual variability in the Kuroshio extension jet speed in an eddy-resolving OGCM.
1033 *Journal of Climate*, 25(10), 3645–3652. <https://doi.org/10.1175/JCLI-D-11-00641.1>

1034 Nonaka, M., Sasai, Y., Sasaki, H., Taguchi, B., & Nakamura, H. (2016). How potentially
1035 predictable are midlatitude ocean currents? *Scientific Reports*, 6(August 2015), 1–8.
1036 <https://doi.org/10.1038/srep20153>

1037 Nonaka, M., Sasaki, H., Taguchi, B., & Schneider, N. (2020). Atmospheric-Driven and Intrinsic
1038 Interannual-to-Decadal Variability in the Kuroshio Extension Jet and Eddy Activities.
1039 *Frontiers in Marine Science*. <https://doi.org/10.3389/fmars.2020.547442>

1040 Ohishi, S., Katsura, S., & Aiki, H. (2019). Salinity frontogenesis/frontolysis in the northeastern
1041 subtropical Pacific region. *Climate Dynamics*, 53(9–10), 5927–5943.
1042 <https://doi.org/10.1007/s00382-019-04907-w>

1043 Oka, E., & Qiu, B. (2012). Progress of North Pacific mode water research in the past decade.
1044 *Journal of Oceanography*, 68(1), 5–20. <https://doi.org/10.1007/s10872-011-0032-5>

1045 Oka, E., Qiu, B., Kouketsu, S., Uehara, K., & Suga, T. (2012). Decadal seesaw of the Central
1046 and Subtropical Mode Water formation associated with the Kuroshio Extension variability.
1047 *Journal of Oceanography*, 68(2), 355–360. <https://doi.org/10.1007/s10872-011-0098-0>

1048 Pak, G., Park, Y.-H., Vivier, F., Bourdallé-Badie, R., Garric, G., & Chang, K.-I. (2017). Upper-
1049 ocean thermal variability controlled by ocean dynamics in the Kuroshio–Oyashio Extension
1050 region. *Journal of Geophysical Research: Oceans*, 122(2), 1154–1176.

1051 <https://doi.org/10.1002/2016JC012076>

1052 Paulson, C. A., & Simpson, J. J. (1977). Irradiance measurements in the upper ocean. *Journal of*
1053 *Physical Oceanography*, 7(6), 952–956. <https://doi.org/10.1175/1520->
1054 0485(1977)007<0952:IMITUO>2.0.CO;2

1055 Pierini, S. (2006). A Kuroshio extension system model study: Decadal chaotic self-sustained
1056 oscillations. *Journal of Physical Oceanography*, 36(8), 1605–1625.
1057 <https://doi.org/10.1175/JPO2931.1>

1058 Pierini, S., Dijkstra, H. A., & Riccio, A. (2009). A nonlinear theory of the Kuroshio extension
1059 bimodality. *Journal of Physical Oceanography*, 39(9), 2212–2229.
1060 <https://doi.org/10.1175/2009JPO4181.1>

1061 Qiu, B. (2000). Interannual Variability of the Kuroshio Extension System and Its Impact on the
1062 Wintertime SST Field. *Journal of Physical Oceanography*, 30(6), 1486–1502.
1063 [https://doi.org/10.1175/1520-0485\(2000\)030<1486:IVOTKE>2.0.CO;2](https://doi.org/10.1175/1520-0485(2000)030<1486:IVOTKE>2.0.CO;2)

1064 Qiu, B. (2002). The Kuroshio Extension system: Its large-scale variability and role in the
1065 midlatitude ocean-atmosphere interaction. *Journal of Oceanography*, 58(1), 57–75.
1066 <https://doi.org/10.1023/A:1015824717293>

1067 Qiu, B., & Chen, S. (2005). Variability of the Kuroshio Extension jet, recirculation gyre, and
1068 mesoscale eddies on decadal time scales. *Journal of Physical Oceanography*, 35(11), 2090–
1069 2103. <https://doi.org/10.1175/JPO2807.1>

1070 Qiu, B., & Chen, S. (2010). Eddy-mean flow interaction in the decadal modulating Kuroshio
1071 Extension system. *Deep Sea Research Part II: Topical Studies in Oceanography*, 57(13–14),
1072 1098–1110. <https://doi.org/10.1016/j.dsr2.2008.11.036>

1073 Qiu, B., & Kelly, K. A. (1993). Upper-Ocean heat balance in the Kuroshio Extension region.
1074 *Journal of Physical Oceanography*, 23(9), 2027–2041. <https://doi.org/10.1175/1520->
1075 0485(1993)023<2027:UOHBIT>2.0.CO;2

1076 Qiu, B., Chen, S., Hacker, P., Hogg, N. G., Jayne, S. R., & Sasaki, H. (2008). The Kuroshio
1077 Extension Northern recirculation gyre: Profiling float measurements and forcing mechanism.
1078 *Journal of Physical Oceanography*, 38(8), 1764–1779.
1079 <https://doi.org/10.1175/2008JPO3921.1>

1080 Qiu, B., Chen, S., & Schneider, N. (2017). Dynamical links between the decadal variability of
1081 the Oyashio and Kuroshio Extensions. *Journal of Climate*, 30(23), 9591–9605.

1082 <https://doi.org/10.1175/JCLI-D-17-0397.1>

1083 Roden, G. I. (1972). Temperature and salinity fronts at the boundaries of the subarctic-
 1084 subtropical transition zone in the western Pacific. *Journal of Geophysical Research*, 77(36),
 1085 7175–7187. <https://doi.org/10.1029/JC077i036p07175>

1086 Roemmich, D., & Gilson, J. (2009). The 2004–2008 mean and annual cycle of temperature,
 1087 salinity, and steric height in the global ocean from the Argo Program. *Progress in*
 1088 *Oceanography*, 82(2), 81–100. <https://doi.org/10.1016/j.pocean.2009.03.004>

1089 Saito, H., Suga, T., Hanawa, K., & Watanabe, T. (2007). New type of pycnostad in the western
 1090 subtropical-subarctic transition region of the North Pacific: Transition Region Mode Water.
 1091 *Journal of Oceanography*, 63(4), 589–600. <https://doi.org/10.1007/s10872-007-0052-3>

1092 Sasaki, Y. N., & Minobe, S. (2015). Climatological mean features and interannual to decadal
 1093 variability of ring formations in the Kuroshio Extension region. *Journal of Oceanography*,
 1094 71(5), 499–509. <https://doi.org/10.1007/s10872-014-0270-4>

1095 Schneider, N., Miller, A. J., & Pierce, D. W. (2002). Anatomy of North Pacific decadal
 1096 variability. *Journal of Climate*, 15(6), 586–605. [https://doi.org/10.1175/1520-0442\(2002\)015<0586:AONPDV>2.0.CO;2](https://doi.org/10.1175/1520-0442(2002)015<0586:AONPDV>2.0.CO;2)

1098 Seager, R., Kushnir, Y., Naik, N. H., Cane, M. A., & Miller, J. (2001). Wind-driven shifts in the
 1099 latitude of the Kuroshio–Oyashio extension and generation of SST anomalies on decadal
 1100 timescales. *Journal of Climate*, 14(22), 4249–4265. [https://doi.org/10.1175/1520-0442\(2001\)014<4249:WDSITL>2.0.CO;2](https://doi.org/10.1175/1520-0442(2001)014<4249:WDSITL>2.0.CO;2)

1102 Smirnov, D., Newman, M., Alexander, M. A., Kwon, Y. O., & Frankignoul, C. (2015).
 1103 Investigating the local atmospheric response to a realistic shift in the Oyashio sea surface
 1104 temperature front. *Journal of Climate*, 28(3), 1126–1147. <https://doi.org/10.1175/JCLI-D-14-00285.1>

1106 Suga, T., Takei, Y., & Hanawa, K. (1997). Thermostad distribution in the North Pacific
 1107 subtropical gyre: The central mode water and the subtropical mode water. *Journal of*
 1108 *Physical Oceanography*, 27(1), 140–152. [https://doi.org/10.1175/1520-0485\(1997\)027<0140:TDITNP>2.0.CO;2](https://doi.org/10.1175/1520-0485(1997)027<0140:TDITNP>2.0.CO;2)

1110 Suga, T., Motoki, K., Aoki, Y., & Macdonald, A. M. (2004). The North Pacific climatology of
 1111 winter mixed layer and mode Waters. *Journal of Physical Oceanography*, 34(1), 3–22.
 1112 [https://doi.org/10.1175/1520-0485\(2004\)034<0003:TNPCOW>2.0.CO;2](https://doi.org/10.1175/1520-0485(2004)034<0003:TNPCOW>2.0.CO;2)

- 1113 Sugimoto, S., & Hanawa, K. (2011). Roles of SST anomalies on the wintertime turbulent heat
1114 fluxes in the kuroshio-oyashio confluence region: Influences of warm eddies detached from
1115 the kuroshio extension. *Journal of Climate*, *24*(24), 6551–6561.
1116 <https://doi.org/10.1175/2011JCLI4023.1>
- 1117 Sugimoto, S., Takahashi, N., & Hanawa, K. (2013). Marked freshening of North Pacific
1118 subtropical mode water in 2009 and 2010: Influence of freshwater supply in the 2008 warm
1119 season. *Geophysical Research Letters*, *40*(12), 3102–3105.
1120 <https://doi.org/10.1002/grl.50600>
- 1121 Sugimoto, S., Kobayashi, N., & Hanawa, K. (2014). Quasi-decadal variation in intensity of the
1122 western part of the winter subarctic SST front in the Western North Pacific: The influence
1123 of Kuroshio extension path state. *Journal of Physical Oceanography*, *44*(10), 2753–2762.
1124 <https://doi.org/10.1175/JPO-D-13-0265.1>
- 1125 Taguchi, B., Xie, S.-P., Schneider, N., Nonaka, M., Sasaki, H., & Sasai, Y. (2007). Decadal
1126 variability of the Kuroshio Extension: Observations and an eddy-resolving model hindcast.
1127 *Journal of Climate*, *20*(11), 2357–2377. <https://doi.org/10.1175/JCLI4142.1>
- 1128 Taguchi, B., Qiu, B., Nonaka, M., Sasaki, H., Xie, S.-P., & Schneider, N. (2010). Decadal
1129 variability of the Kuroshio Extension: mesoscale eddies and recirculations. *Ocean
1130 Dynamics*, *60*(3), 673–691. <https://doi.org/10.1007/s10236-010-0295-1>
- 1131 Taguchi, B., Nakamura, H., Nonaka, M., Komori, N., Kuwano-Yoshida, A., Takaya, K., & Goto,
1132 A. (2012). Seasonal evolutions of atmospheric response to decadal SST anomalies in the
1133 North Pacific subarctic frontal zone, observations and a coupled model simulation. *Journal
1134 of Climate*, *25*(1), 111–139. <https://doi.org/10.1175/JCLI-D-11-00046.1>
- 1135 Tanimoto, Y., Nakamura, H., Kagimoto, T., & Yamane, S. (2003). An active role of extratropical
1136 sea surface temperature anomalies in determining anomalous turbulent heat flux. *Journal of
1137 Geophysical Research*, *108*(C10), 3304. <https://doi.org/10.1029/2002JC001750>
- 1138 Tomita, H., Hihara, T., Kako, S., Kubota, M., & Kutsuwada, K. (2019). An introduction to J-
1139 OFURO3, a third-generation Japanese ocean flux data set using remote-sensing
1140 observations. *Journal of Oceanography*, *75*(2), 171–194. [https://doi.org/10.1007/s10872-
1141 018-0493-x](https://doi.org/10.1007/s10872-018-0493-x)
- 1142 Tsujino, H., Usui, N., & Nakano, H. (2006). Dynamics of Kuroshio path variations in a high-
1143 resolution general circulation model. *Journal of Geophysical Research*, *111*, C11001.

1144 <https://doi.org/10.1029/2005JC003118>

1145 Usui, N., Fujii, Y., Sakamoto, K., & Kamachi, M. (2015). Development of a four-dimensional
 1146 variational assimilation system for coastal data assimilation around Japan. *Monthly Weather*
 1147 *Review*, *143*(10), 3874–3892. <https://doi.org/10.1175/MWR-D-14-00326.1>

1148 Usui, N., Wakamatsu, T., Tanaka, Y., Hirose, N., Toyoda, T., Nishikawa, S., et al. (2017). Four-
 1149 dimensional variational ocean reanalysis: a 30-year high-resolution dataset in the western
 1150 North Pacific (FORA-WNP30). *Journal of Oceanography*, *73*(2), 205–233.
 1151 <https://doi.org/10.1007/s10872-016-0398-5>

1152 Vialard, J., & Delecluse, P. (1998). An OGCM Study for the TOGA decade. Part I: Role of
 1153 salinity in the physics of the Western Pacific fresh pool. *Journal of Physical Oceanography*,
 1154 *28*(6), 1071–1088. [https://doi.org/10.1175/1520-0485\(1998\)028<1071:AOSFTT>2.0.CO;2](https://doi.org/10.1175/1520-0485(1998)028<1071:AOSFTT>2.0.CO;2)

1155 Vivier, F., Kelly, K. A., & Thompson, L. A. (2002). Heat budget in the Kuroshio extension
 1156 region: 1993-99. *Journal of Physical Oceanography*, *32*(12), 3436–3454.
 1157 [https://doi.org/10.1175/1520-0485\(2002\)032<3436:HBITKE>2.0.CO;2](https://doi.org/10.1175/1520-0485(2002)032<3436:HBITKE>2.0.CO;2)

1158 Wagawa, T., Ito, S. I., Shimizu, Y., Kakehi, S., & Ambe, D. (2014). Currents associated with the
 1159 quasi-stationary jet separated from the Kuroshio extension. *Journal of Physical*
 1160 *Oceanography*, *44*(6), 1636–1653. <https://doi.org/10.1175/JPO-D-12-0192.1>

1161 Yan, Y., Chassignet, E. P., Qi, Y., & Dewar, W. K. (2013). Freshening of subsurface waters in
 1162 the northwest pacific subtropical gyre: Observations and dynamics. *Journal of Physical*
 1163 *Oceanography*, *43*(12), 2733–2751. <https://doi.org/10.1175/JPO-D-13-03.1>

1164 Yang, Y., San Liang, X., Qiu, B., & Chen, S. (2017). On the decadal variability of the eddy
 1165 kinetic energy in the Kuroshio extension. *Journal of Physical Oceanography*, *47*(5), 1169–
 1166 1187. <https://doi.org/10.1175/JPO-D-16-0201.1>

1167 Yasuda, I. (2003). Hydrographic structure and variability in the Kuroshio-Oyashio Transition
 1168 Area. *Journal of Oceanography*, *59*(4), 389–402.
 1169 <https://doi.org/https://doi.org/10.1023/A:1025580313836>

1170 Yasuda, T., & Hanawa, K. (1997). Decadal changes in the mode waters in the midlatitude North
 1171 Pacific. *Journal of Physical Oceanography*. [https://doi.org/10.1175/1520-](https://doi.org/10.1175/1520-0485(1997)027<0858:DCITMW>2.0.CO;2)
 1172 [0485\(1997\)027<0858:DCITMW>2.0.CO;2](https://doi.org/10.1175/1520-0485(1997)027<0858:DCITMW>2.0.CO;2)

1173 Yuan, X., & Talley, L. D. (1996). The subarctic frontal zone in the North Pacific: Characteristics
 1174 of frontal structure from climatological data and synoptic surveys. *Journal of Geophysical*

1175 *Research: Oceans*, 101(C7), 16491–16508. <https://doi.org/10.1029/96JC01249>

1176 Zhang, Y., Du, Y., & Qu, T. (2016). A sea surface salinity dipole mode in the tropical Indian
1177 Ocean. *Climate Dynamics*, 47(7–8), 2573–2585. <https://doi.org/10.1007/s00382-016-2984-z>

1178 Zheng, F., & Zhang, R.-H. (2012). Effects of interannual salinity variability and freshwater flux
1179 forcing on the development of the 2007/08 La Niña event diagnosed from Argo and satellite
1180 data. *Dynamics of Atmospheres and Oceans*, 57, 45–57.
1181 <https://doi.org/10.1016/j.dynatmoce.2012.06.002>

1182 Zheng, F., & Zhang, R.-H. (2015). Interannually varying salinity effects on ENSO in the tropical
1183 Pacific: A diagnostic analysis from Argo. *Ocean Dynamics*, 65(5), 691–705.
1184 <https://doi.org/10.1007/s10236-015-0829-7>

1185 Zhu, J., Huang, B., Zhang, R.-H., Hu, Z.-Z., Kumar, A., Balmaseda, M. A., et al. (2015). Salinity
1186 anomaly as a trigger for ENSO events. *Scientific Reports*, 4, 6821.
1187 <https://doi.org/10.1038/srep06821>

1188